Direct observations of microscale turbulence and thermohaline structure in the Kuroshio Front

Takeyoshi Nagai,[1] Amit Tandon,[2] Hidekatsu Yamazaki,[1] Mark J. Doubell,[3] and Scott Gallager[4]

Received 17 April 2011; revised 12 June 2012; accepted 19 June 2012; published 9 August 2012.

[1] Direct observations of microstructure near the Kuroshio Front were conducted in August 2008 and October 2009. These show negative potential vorticity (PV) in the mixed layer south of the front, where directly measured turbulent kinetic energy dissipation rates are an order magnitude larger than predicted by wind-scaling. These elevated dissipation rates scale better with an empirical scaling, which considers local wind and Ekman buoyancy flux driven by downfront wind. Near-zero PV in the thermocline under the Kuroshio mainstream is observed at 200–300 m depth, with dissipation exceeding open ocean thermocline values by factors of 10–100. Overall, the large turbulent dissipation rates measured in the Kuroshio can be categorized into two groups, one characterized by low Richardson number along the Kuroshio Front thermocline, and the other characterized by high stratification away from the Kuroshio mainstream. The former is attributed to mixing by unbalanced frontal ageostrophic flows, and the latter is attributed to internal wave breaking. On average, both groups appear in regions of large horizontal density gradients. Observed thermohaline structure shows low salinity tongues from the surface to over 300 m depth and deep cold tongues, extending upward from 500 to 100 m depth in a narrow (20 km) zone, suggesting down and upwelling driven by geostrophic straining, which is confirmed by Quasigeostrophic-Omega equation solutions. This implies that adiabatic along isopycnal subduction and diabatic diapycnal turbulent mixing acting in tandem at the Kuroshio Front likely contribute to NPIW formation.

Citation: Nagai, T., A. Tandon, H. Yamazaki, M. J. Doubell, and S. Gallager (2012), Direct observations of microscale turbulence and thermohaline structure in the Kuroshio Front, *J. Geophys. Res.*, *117*, C08013, doi:10.1029/2011JC007228.

1. Introduction

[2] Fronts in the ocean are known as sites of vigorous subduction and upwelling caused by meso- and submesoscale straining due to eddies around fronts, meandering of fronts themselves [*Hoskins and Bretherton*, 1972; *Pollard and Regier*, 1992; *Rudnick*, 1996], as well as frictional Ekman suction and pumping due to wind-forcing, or internal friction in absence of the wind [*Thompson*, 2000; *Thomas and Lee*, 2005; *Nagai et al.*, 2006; *Giordani et al.*, 2006]. Since the vertical transport in the frontal regions brings nutrient rich water from lower layers into euphotic zone, fronts are also known to be sites of high biological productivity [*Franks and Walstad*, 1997], and therefore, as fertile fishing grounds [*Uda*, 1936].

[3] The ageostrophic circulation near a front has been traditionally inferred using inviscid balanced equations, such as Quasigeostrophic (QG) and Semigeostrophic (SG) Omega equations. These imply a downwelling tendency on the dense side and upwelling on the buoyant side of the front during frontogenesis and vice versa for frontolysis [*Pollard and Regier*, 1992; *Rudnick*, 1996]. The QG-ω equation is known to fail under high curvature and/or large Rossby numbers, which can be remedied using SG framework, although the potential vorticity needs to retain a uniform sign so that the equation remains elliptic. The vertical flows diagnosed using QG-ω equation typically have broad horizontal scale $>\mathcal{O}$ (10 km), with maximum magnitude of $\mathcal{O}$(10 m day^{-1}) at intermediate depth (>100 m depth).

[4] In contrast, recent high-resolution numerical studies using idealized frontal setups have revealed that intense upwelling and subduction occur near the surface in submesoscale range, $\mathcal{O}$(100 m)–$\mathcal{O}$(1 km) [*Mahadevan and Archer*, 2000; *Lévy et al.*, 2001], which is found to be associated with restratifying nature of surface mixed layer fronts [*Boccaletti et al.*, 2007; *Fox-Kemper and Ferrari*,

[1]Department of Ocean Sciences, Tokyo University of Marine Science and Technology, Tokyo, Japan.
[2]SMAST/Physics Department, University of Massachusetts Dartmouth, North Dartmouth, Massachusetts, USA.
[3]South Australian Aquatic Sciences Centre, SARDI Aquatic Sciences, Henley Beach, South Australia, Australia.
[4]Woods Hole Oceanographic Institution, Woods Hole, Massachusetts, USA.

Corresponding author: T. Nagai, Department of Ocean Sciences, Tokyo University of Marine Science and Technology, 4-5-7 Konan Minato-ku, Tokyo 108-8477, Japan. (tnagai@kaiyodai.ac.jp)

0148-0227/12/2011JC007228

2008; *Mahadevan et al.*, 2010]. These near surface features can possibly interact with deep adiabatic regime of ageostrophic flows driven by the mesoscale straining (E. Holmes and A. Tandon, personal communication, 2010), and wind and/or frictionally induced ageostrophic secondary circulation [*Thomas and Ferrari*, 2008; *Mahadevan et al.*, 2010; *Nagai et al.*, 2006; *Giordani et al.*, 2006]. Recent theoretical studies have also suggested that unbalanced flows near the fronts eventually break into inertia-gravity waves and/or three-dimensional microscale turbulence, which cascade mesoscale energy down to the Kolmogorov scale, where energy is finally dissipated to heat [*McWilliams*, 2008; *Molemaker et al.*, 2010; *Capet et al.*, 2008a, 2008b, 2008c]. Generation mechanisms of such unbalanced flows have been proposed as follows. *Molemaker et al.* [2005] showed that the anticyclonic ageostrophic instability can grow when $f+\zeta-S<0$, where f is Coriolis parameter, ζ is vertical component of relative vorticity, and the strain rate, S is defined as $\sqrt{(u_x-v_y)^2+(v_x+u_y)^2}$. This is a less severe constraint than the condition of inertial instability, $f+\zeta<0$. The anticyclonic ageostrophic instability condition can be satisfied even in QG flows especially on anticyclonic side of the front. On the other hand, *McWilliams et al.* [2009] showed that two-dimensional baroclinic ageostrophic frontogenesis caused by barotropic confluence results in growth of three-dimensional high wave number velocity fluctuations, and is potentially another route to dissipation [*Capet et al.*, 2008a, 2008b, 2008c; *Molemaker et al.*, 2010]. In addition, another route is via the symmetric instability, which can grow when slope of the isopycnal is steeper than the slope of the isosurface of absolute momentum, which is equivalent to the condition that materially invariant Ertel potential vorticity (PV) has different signs in the domain. Symmetrically unstable condition can efficiently arise near the front by destruction of the PV due to downfront wind (winds in the same direction of the frontal current), which induces Ekman buoyancy flux, and brings heavier water over lighter water across the front [*Thomas and Ferrari*, 2008]. A numerical study by *Taylor and Ferrari* [2009] suggests that the secondary Kelvin-Helmholtz instability following the symmetric instability can efficiently achieve equilibrium by three-dimensional turbulence, which with the downfront wind [*Thomas and Taylor*, 2010] and buoyancy flux [*Taylor and Ferrari*, 2010], enhance the extraction of geostrophic kinetic energy to turbulent dissipation. Several previous studies have also pointed out that the wind-forcing and near-surface turbulent friction and mixing [*Thompson*, 2000; *Nagai et al.*, 2006, 2008; *Pallás-Sanz et al.*, 2010a, 2010b; *Giordani et al.*, 2006] and that in the interior [*Garrett and Loder*, 1981] of the ocean fronts could induce ageostrophic secondary flows, in addition to that arisen from confluence and diffluence [*Hoskins and Bretherton*, 1972].

[5] Though confluence and wind-forcing play an important role in driving ageostrophic secondary circulation, it is unclear whether this would result in enhanced dissipation at the fronts. There is some observational evidence to support enhanced mixing near fronts. Microstructure observations in the California Current System by *Dewey and Moum* [1990] have shown strong turbulent dissipation near the surface, which had deeper extent on the warm side of the front reflecting deeper mixed layer compared to that on the strongly stratified cold side of the front. Similar tendency is seen in our observations near the surface. A number of recent high-resolution observations have found symmetrically unstable negative PV regions in the mixed layer formed through PV destruction by the downfront wind in the subpolar front of Japan/East Sea [*Thomas and Lee*, 2005], and in the Kuroshio Front [*D'Asaro et al.*, 2011]. The latter study observed elevated turbulent dissipation in the mixed layer at the sharpest part of the Kuroshio Front, using a Lagrangian float. This observed enhanced turbulent dissipation is attributed to strong confluent flow formed by the Kuroshio and the Oyashio currents, and the Ekman buoyancy flux due to the downfront wind [*D'Asaro et al.*, 2011].

[6] Below the mixed layer, turbulence has traditionally been believed to be very weak even near fronts, which have large current shear, as it is always compensated by strong stratification. A number of field studies using microstructure profilers in 1970's concluded that moderate levels of patchy turbulence measured near the Gulf Stream are attributed to random internal wave breaking [*Oakey and Elliot*, 1977; *Gregg and Sanford*, 1980], supporting the above notion. However, recent microstructure experiments in the Gulf Stream [*Winkel et al.*, 2002; *Inoue et al.*, 2010] observed banded shear with alternating signs under the Gulf Stream and showed that turbulent kinetic energy dissipation rates in the thermocline of the Gulf Stream were an order of magnitude larger than typical thermocline dissipation rates in the open ocean. These studies attributed the observed turbulence entirely to internal wave breaking. In contrast, *Nagai et al.* [2009] observed strong turbulent dissipation rates, $\mathcal{O}(10^{-7})$ Wkg^{-1} with strong ageostrophic shear in the thermocline under the frontogenetic Kuroshio mainstream at 200–250 m depth. As the directly observed strong turbulence was on the cyclonic side of the jet, where the wall of positive effective Coriolis parameter may reflect near inertial waves, it was suggested that breaking of remotely generated near inertial waves were unlikely to be the source of the observed turbulence. Instead, because strong turbulence is found away from the surface boundary layer, they suggested that the unforced, unbalanced route to dissipation could be active in the Kuroshio thermocline, although the number of measured dissipation profiles was rather small [*Nagai et al.*, 2009]. Similarly, *Johnston et al.* [2011] reported elevated turbulent dissipation on the cyclonic side of the fronts off California Current System using a towed high-resolution microconductivity profiler.

[7] Although observational evidence of enhanced turbulence near fronts has increased, the detailed mechanisms responsible for increased dissipation and their relative importance is still unclear. Specifically, it is unknown whether the dominant dissipation mechanism near fronts occur through mesoscale confluence-induced loss of balance in QG (or SG) flows, breaking of near-inertial waves trapped by the geostrophic vorticity field [*Kunze*, 1985] or PV reduction forced by downfront wind and/or buoyancy flux. Additional observations with particular emphasis on the turbulent dissipation, confluence, and surface forcing near the front are required to assess this issue. In this study, data from a series of intensive field campaigns of microstructure observations conducted in summer 2008 and fall 2009 with multiple north–south sections near the Kuroshio Front are analyzed. The objectives of this study are (1) to characterize thermohaline structure and

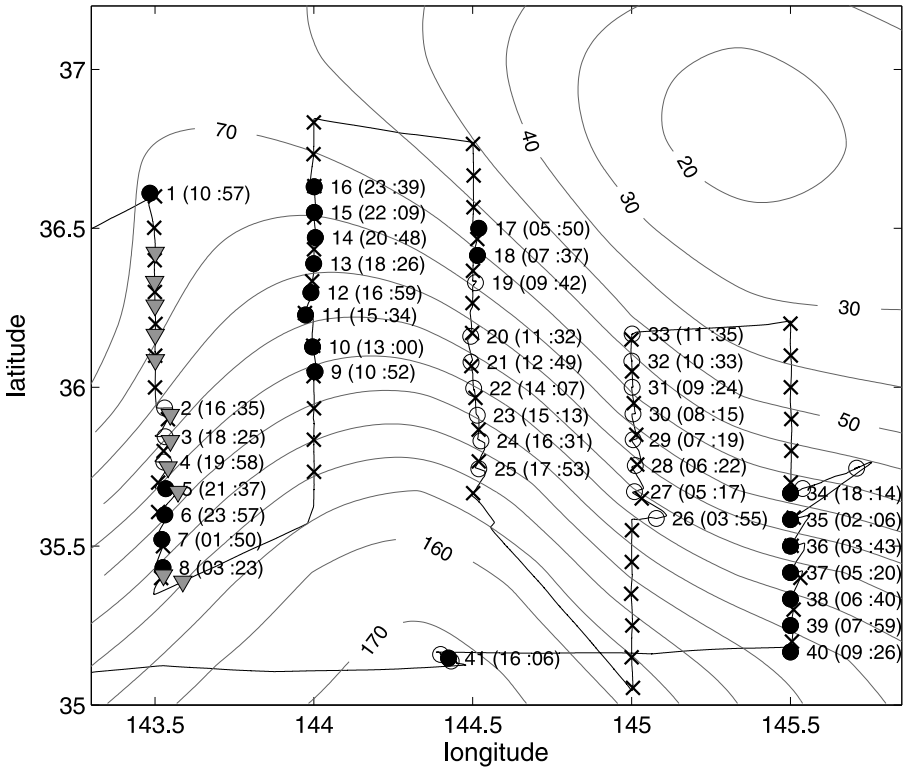

Figure 1. Observational stations of 2009 surveys in Oct. 17–24. Solid line shows trajectory of R.V. Natsushima. Contours indicate mapped delayed time absolute dynamic topography (cm) on Oct 21, 2009 available from AVISO. Numbers indicate CTD station number, and time of the day is shown in brackets. Crosses are XBT stations every 11.1 km, open circles are CTD stations every 9.26 km without TurboMAP, solid circles are CTD stations with TurboMAP deployment, and triangles are underway CTD stations.

microscale turbulence, (2) to elucidate whether turbulent dissipation is enhanced near the Kuroshio Front, (3) to investigate generation mechanisms of observed microscale turbulence, and (4) to infer ageostrophic vertical flow.

[8] The paper is organized as follows: Section 2 describes the observations and data analysis; section 3 discusses low salinity tongues extending from the top and cold temperature tongues from depth to upper layers near the Kuroshio Front within 20 km of each other, followed by results of the microstructure measurements in the mixed layer and below the mixed layer. Section 4 investigates mesoscale forcing and vertical flow inferred using QG-ω equation. Section 5 summarizes the results.

2. Field Experiments and Data Analysis

[9] An intensive interdisciplinary field campaign was carried out using R/V Natsushima (JAMSTEC) from October 17 through 24, 2009. We made five north–south transects, each of which spans about 140 km. The western most transect is named as Leg A, followed by Leg B and so on to Leg E, which is the most eastward (Figure 1). We deployed CTD (Advantech Ltd.) with Niskin Bottles, Lowered Acoustic Doppler Current Profiler (LADCP) (300 kHz), and Visual Plankton Recorder (VPR) every 9.26 km (5 miles) at 7–9 stations for each north–south transect to approximately 275 m depth. LADCP was programmed to average velocity data over 10 m with 20 bins and at 1 Hz. Each standard CTD/LADCP profile takes about 40 minutes for deployment and recovery. In addition to the conventional CTD observations, towed, free-fall CTD, Underway CTD (Oceanscience) was also deployed at 11 stations along Leg A. Every 11.1 km (6 miles), XBT (T-7) observations were conducted at 12 stations for each transect to acquire mesoscale temperature field across and along front. XBT observations at each station yielded a vertical temperature profile down to 750 m depth. Turbulence Ocean Microstructure Acquisition Profiler Laser (TurboMAP-L) [*Doubell et al.*, 2009] was deployed at 2–8 stations for each transect (except Leg D due to a technical problem). Acoustic backscatter was measured by SIMRAD EK60 with two frequencies, 38 kHz and 120 kHz.

[10] The observed CTD measurements are used to correct the depth of the LADCP, and velocity profiles are obtained utilizing the shear method [*Fischer and Visbeck*, 1993], implemented in the freely available LDEO LADCP Processing software developed by A.M. Thurnherr (http://www.ldeo.columbia.edu/ ant/LADCP/). The LADCP data are referenced to the surface flow measured by a shipboard surface Doppler current meter. As most of our CTD data are recorded during their downcasts, we extract the velocity profile derived only from downcast data.

[11] The turbulent kinetic energy dissipation rates for 2008 and 2009 data are estimated by integrating shear

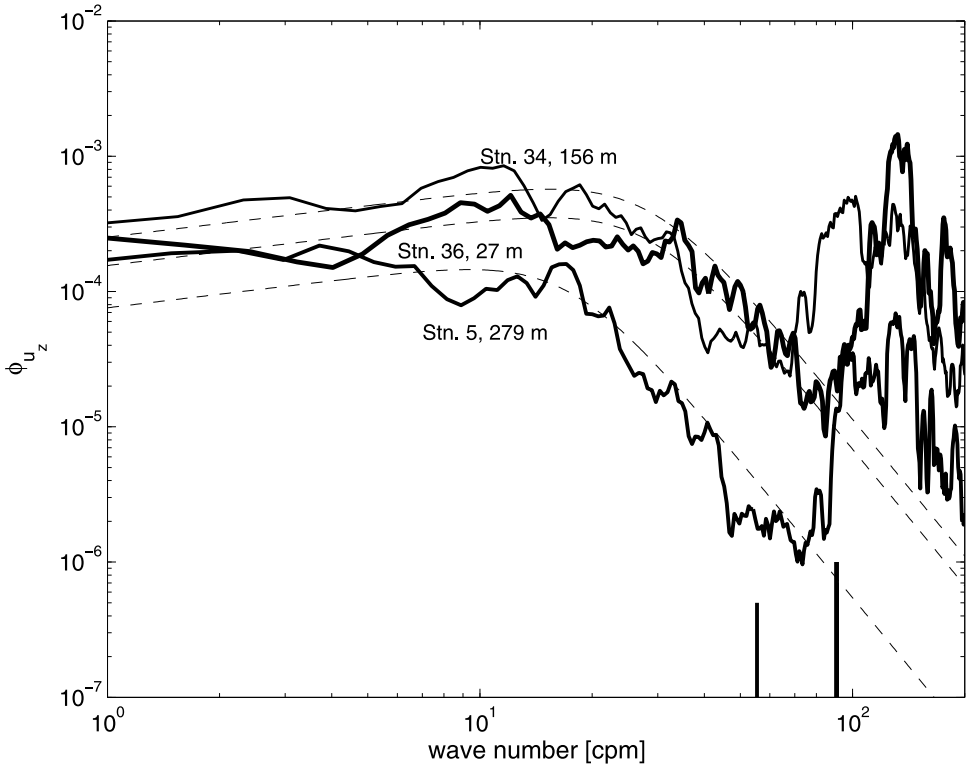

Figure 2. Turbulent shear spectra (solid curves) and Nasmyth shear spectra (broken lines) are shown for 279 m depth at Stn. 5 in Leg A (solid line), 46 m depth at Stn. 36 in Leg E (thick solid line), and 156 m depth at Stn. 34 in Leg E (thin solid line) near the low PV waters above and below the mixed layer depth. The dissipation rates obtained are, 2.9×10^{-8}, 8.5×10^{-8}, and 1.8×10^{-7} Wkg^{-1} for Stn. 5, Stn. 36, and Stn. 34, respectively. Note that in Stn. 34, the high wave number shear variance is not well resolved even after the response correction of *Oakey* [1982] is employed. Vertical lines indicate Kolmogorov wave numbers, k_s for each station with the same line widths. The k_s for Stn 34 and 36 are indistinguishable in log scale.

spectrum between roughly 1 cpm and the half of the Kolmogorov wave number, where shear spectra agree well with the Nasmyth shear spectrum (Figure 2). Beyond this range in wave number, we extrapolate shear spectra using the Nasmyth spectrum to avoid integrating noise spectra. A correction for the Nasmyth spectrum proposed by *Oakey* [1982] is employed for unresolved high wave number shear variance. A single value of dissipation rate is obtained over a 4 m depth bin, corresponding to approximately 3600 data points for shear data.

[12] Measured temperature and salinity data are averaged every 4 m, and velocity data are interpolated on the same depth grid. These 4 m data are used to construct vertical (y-z) sections of temperature, salinity, velocity, and background Richardson number, making use of optimum interpolation with decorrelation scale of 25 km and 40 m for meridional and vertical direction, respectively.

[13] Meteorological data for wind speed, direction, and air temperature are measured continuously during the cruise every 1 minute, and atmospheric pressure and cloudiness recorded every 4 hours. We use relative humidity data available every hour from Choshi meteorological station closest to the observational site. These data are used to estimate net heat flux during nighttime and wind stress using bulk formula developed by *Fairall et al.* [1996].

[14] For similar observations in 2008, we deployed XBT every 3.7 km and TurboMAP-II every 28 km across the Kuroshio Front. Details of these observations can be found in *Nagai et al.* [2009].

3. Microscale Turbulence and Thermohaline Structure Near the Kuroshio Front

[15] Shipboard surface Doppler current meter data and Sea Surface Temperature satellite image show that most of the north–south transects were nearly normal to the Kuroshio Front, which was undergoing small amplitude mesoscale meandering (Figure 3b). Based on the surface current data across the Kuroshio jet, Leg A through C span a region where the mesoscale meander is transitioning from crest to trough, while Leg D and E are in a region which transitions from trough to crest (Figure 3b). The speed of the eastward flowing Kuroshio jet exceeds 2 ms^{-1}. AVHRR SST image (Figure 3) shows that there was a warm water pool to the north of the Leg A and B, which extended northward wrapped around a high sea surface height field clockwise as is typically the case for surface streamers of warm water. The current data near the warm water pool shows clockwise flow, the southern edge of which flows westward, opposite to the Kuroshio Current. This flow pattern is suggestive of

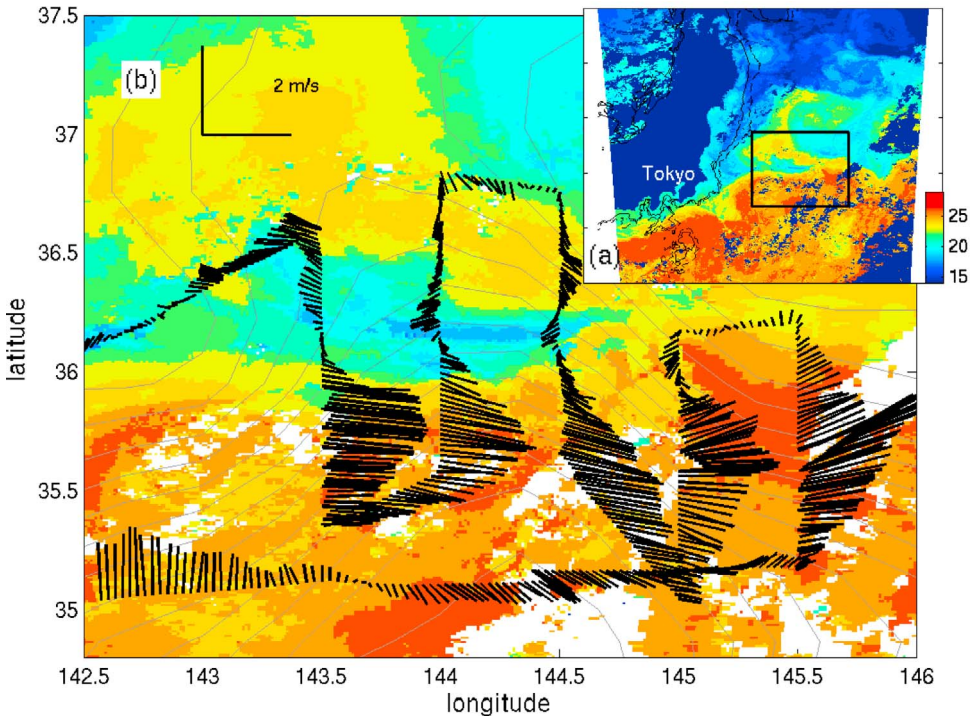

Figure 3. Surface current speed and direction. Color shows NOAA Sea Surface Temperature (°C) of Oct 18. Contours are absolute dynamic topography [cm]. Broken and solid contours in Figure 3a are at 1000 m and 500 m bathymetry isolines, respectively.

submesoscale cyclonic vorticity ($\sim\mathcal{O}$(10 km) between the warm water pool and the Kuroshio Front, in which the flow changes its direction from westward to eastward within 10–20 km scale and is inconsistent with SSH field and appears more correlated with SST. This feature (Figure 3b, Legs B and C) shows flow toward the Kuroshio mainstream, creating a region of confluence. Wind records along the ship track show that wind speed was moderate to strong ($\sim$3–15 ms^{-1}), and wind direction was aligned downfront (in the same direction as the frontal jet) in southern part of Leg A and C, while crossfront or upfront wind (in the opposite direction as the frontal jet) are found in other regions (Figure 4a). Along-front wind component averaged from Leg A through E, with respect to the Kuroshio axis, defined as the location of current maxima, shows that averaged wind to the south of the front was $\sim$5 ms^{-1} and was downfront (Figures 4b and 4c).

[16] One of the most prominent features we observed is a low salinity tongue elongated from the surface to over 300 m depth in Leg A (centered at 35.9°N), which is accompanied by a low temperature tongue extending from below 500 m to 100 m depth (Figure 5). These tongues of two different water properties occur within 20 km in the same location, implying up- and downwelling are strongly modifying tracer

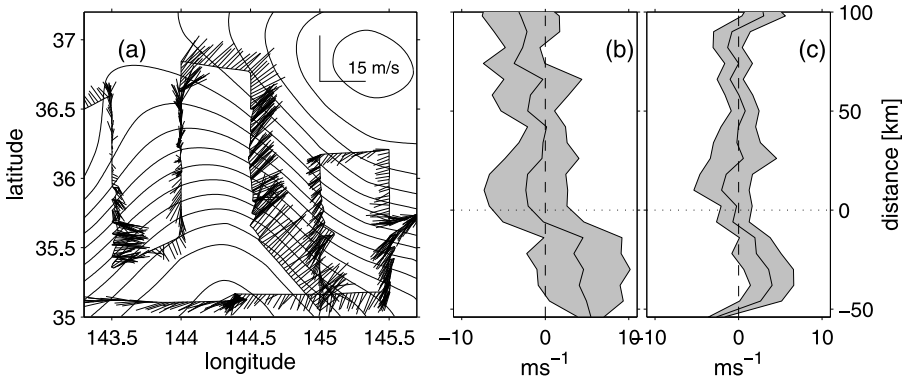

Figure 4. (a) Wind speed and direction. Contours in Figure 4a are absolute dynamic topography [cm]. (b) Along front component of wind speed (ms^{-1}) averaged through Leg A to E, i.e., $W\cos(\theta_{curr} - \theta_{wind})$, where W is wind speed and θ_{curr} and θ_{wind} are current direction of shipboard surface ADCP, and wind direction, respectively. Downfront wind is positive. Shading indicates standard deviation. (c) Same plot as Figure 4b but with θ_{curr} computed from SSH derived geostrophic flow.

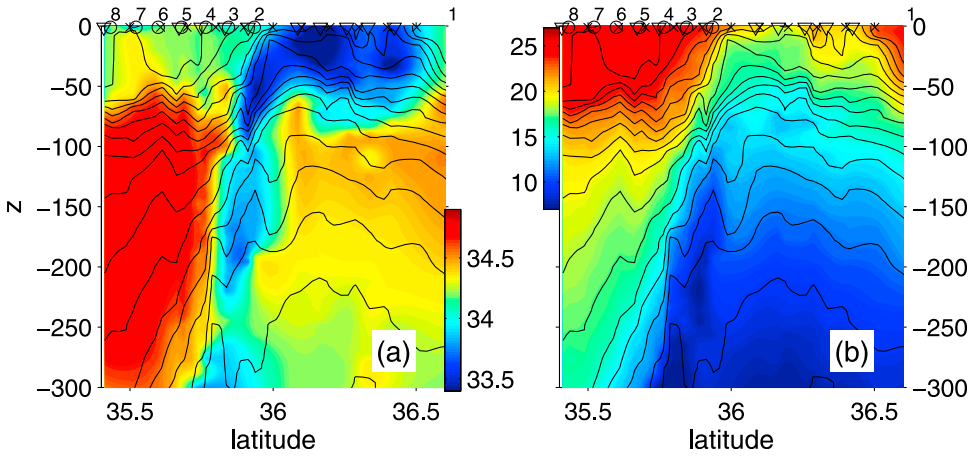

Figure 5. Vertical section of (a) salinity and (b) temperature with black contours of σ_θ every 1 (σ_θ) for 2009 data in Leg A. Above the top abscissa, circles show CTD/LADCP stations, crosses indicate XBT stations, and triangles are for UCTD stations.

distributions. This will be investigated in section 4 using the Quasi-Geostrophic (hereinafter QG) omega equation. Although low salinity water near the Kuroshio mainstream has been observed [e.g., *Iwamatsu et al.*, 2003], it is only after recent high-resolution surveys that tongue like structures from the surface have begun to be confirmed [e.g., *Kouketsu et al.*, 2005]. Low salinity water is found in most of the transects across the Kuroshio, including our 2008 data (Figure 6). It is intriguing that the most of the salinity structures, which concave downward, are accompanied by cold temperature structure, which convex upward in an overlapping depth range (100–300 m). This suggests that diapycnal mixing between low salinity-low temperature and high salinity-high temperature waters is active at the intermediate depths near the Kuroshio Front. These tongues are also suggestive of both upwelling and downwelling occurring in close proximately of the Kuroshio Front (Figures 5 and 6a–6d).

[17] Thermal structure across the Kuroshio Front shows the simultaneous presence of two fronts on the warm side of the Kuroshio with different vertical scales, i.e., the deep Kuroshio Front of the vertical scale, >500 m, and shallow front, ~100 m on top of the Kuroshio Front (Figure 6). Along the isopycnal of the shallow front, a shallow low salinity signature is observed in Leg D and E (Figures 6d and 6e), which is also a tongue of elevated nutrients in Leg E (not shown), suggesting that submesoscale subduction of nutrient-rich north side water could potentially fertilize the oligotrophic Kuroshio water (S. Clayton et al., personal communication, 2010).

3.1. Turbulence in the Mixed Layer Front

[18] The stratification in the upper 100 m is quite different north and south of the Kuroshio Front. The relatively well mixed near-surface water on the southern side of the Kuroshio Front, forms a mixed layer front. In contrast, stronger stratification is found in upper layers on the north side of the front. This may suppress rapid restratification of the mixed layer front [*Fox-Kemper et al.*, 2008] to the north, as the north side of the front is already stratified. This contrast in stratification across the Kuroshio Front influences the across front variations in the vertical extent of the turbulent kinetic energy dissipation rate as in *Dewey and Moum* [1990]. On the north side of the Kuroshio main axis, at Stn.9 and 10 in Leg B, turbulent shear is stronger subsurface at 50–150 m depth, rather than closer to the surface. At these stations, south of the warm water pool, surface features show submesoscale cyclonic vortex structure (Figure 3) and the low salinity water appears right next to the Kuroshio mainstream (Figures 6b and 6c). The dissipation rate of the subsurface turbulence is found to be $\mathcal{O}\left(10^{-8}-10^{-7}\right)$ Wkg^{-1} (Figure 10c). In contrast, intense turbulent shear is observed in the relatively well mixed upper 70 m, on the warm side of the Kuroshio Front for Leg A and Leg E (Figures 6a and 6e), where the dissipation rate is found to be $\mathcal{O}\left(10^{-7}-10^{-6}\right)$ Wkg^{-1} (Figures 10a and 10g).

[19] Measured dissipation rates in the mixed layer during daytime are compared with the wind-scaling for the dissipation, i.e.,

$$\epsilon_W = \frac{u_\star^3}{\kappa z}, \tag{1}$$

where κ is von Karman constant, 0.41, and $u_\star$ is friction velocity, $\sqrt{\tau/\rho}$, where τ is the wind stress. Since the contribution from rapidly flowing surface current of the Kuroshio Current (>2 ms^{-1}) to the momentum stress at the surface may not be negligible, velocity difference between the surface current and wind speed is taken into account using conventional bulk equation [*Fairall et al.*, 1996]. However, accounting for the influence of surface currents in the scaling makes only up to 10% difference. The mixed layer depth, D, defined as the depth at which temperature drops 0.05°C from the surface, is rather shallow (~10 m) north of the front, and relatively deeper (30–60 m) on the south side. Because the dissipation measurements in the near surface region could be influenced from wake of the ship, we only scale the dissipation rate data below 10 m depth. This automatically eliminates dissipation data in Stn. 9–13 of Leg B as the mixed layer depth is quite shallow (<10 m). Normalized and averaged shear spectra in the mixed layer show fairly good agreement with *Nasmyth* [1970] turbulence

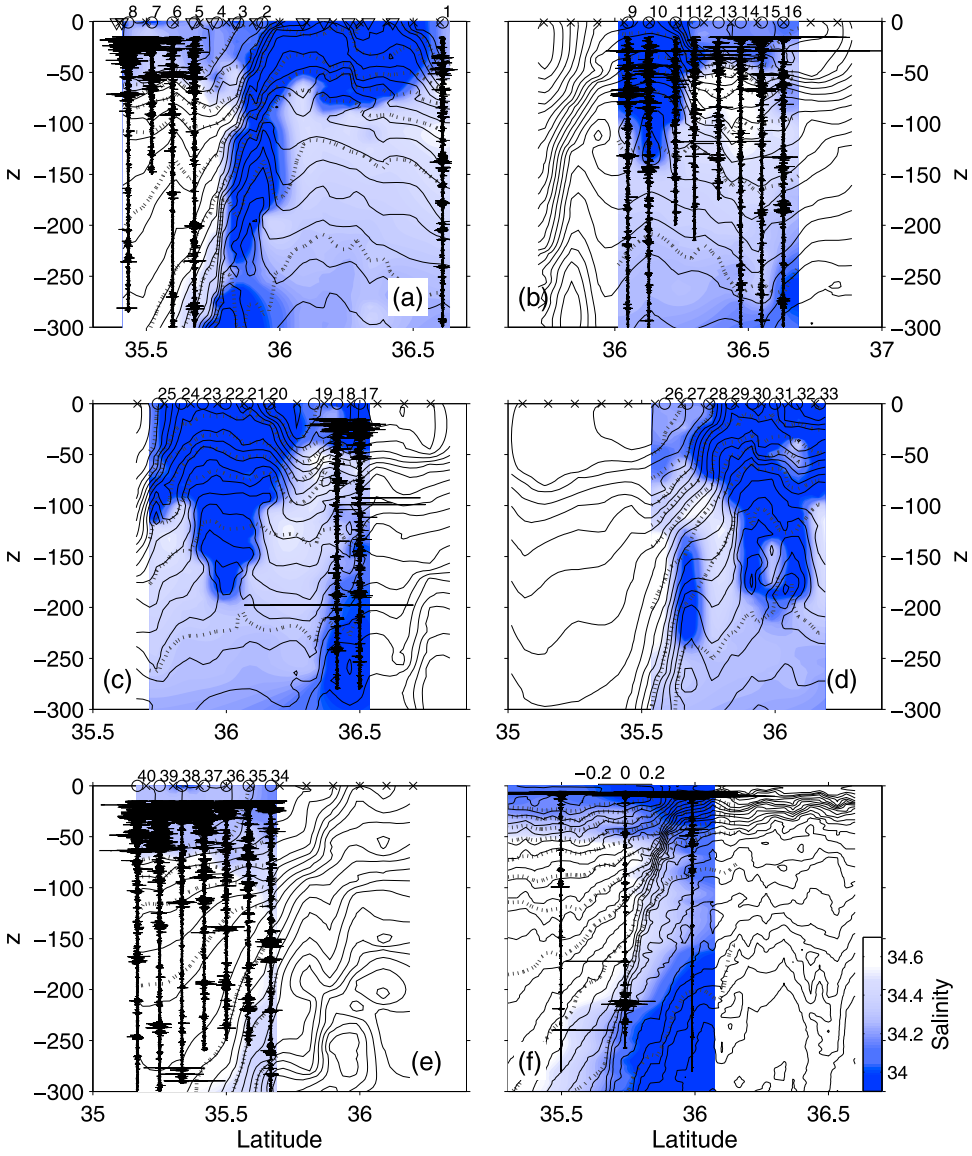

Figure 6. Vertical section of (contour) temperature, and (shading) salinity with turbulent shear data for 2009 data in (a) Leg A, (b) Leg B, (c) Leg C, (d) Leg D, and (e) Leg E and (f) 2008 data. Temperature contours are drawn every 0.25°C. Small scale on top of Figure 6f is for the turbulent shear data (s^{-1}). Above the top abscissa, circles show CTD/LADCP stations, crosses indicate XBT stations, triangles are for UCTD stations, and numbers represents station number. Dashed gray contours are isopycnals every 0.5 σ_θ.

spectra (Figure S1 in the auxiliary material).[1] The scaled daytime dissipation rates in Stn.1 show much weaker values than that based on the wind-scaling. As the observations conducted at Stn.1 are 5–6 hours after sunrise, penetrative solar heating can suppress turbulence, along with modulation of diurnal remnant layer [*Brainerd and Gregg*, 1993]. In contrast, the scaled dissipation rates in Leg E (Stn. 38–40, Figure 7a) are 5 to 10 times greater than that of the wind-scaling, ϵ_W, all through the mixed layer. The elevated dissipation does not follow z^{-4} or z^{-2} power laws (Figure 7a), which have been found for surface wave breaking [*Terray et al.*, 1996]. These stations are on the south side of the Kuroshio Front where relatively deeper mixed layer is formed, and where the cruise averaged wind is in downfront direction (Figures 4b and 4c). *Thomas and Taylor* [2010] showed that under downfront wind conditions, the sum of the turbulent kinetic energy production terms can be scaled by Ekman buoyancy flux (hereinafter, EBF). The large dissipation rates found in Leg E (Stn. 38–40) are, therefore, scaled by EBF (Figures 7b and 7c). EBF is estimated by taking the product of buoyancy gradient and Ekman transport computed with the cruise-averaged downfront wind (Figure 4b), assuming that Ekman drift is fully developed after several inertial periods (note local 2π

[1]Auxiliary materials are available in the HTML. doi:10.1029/2011JC007228.

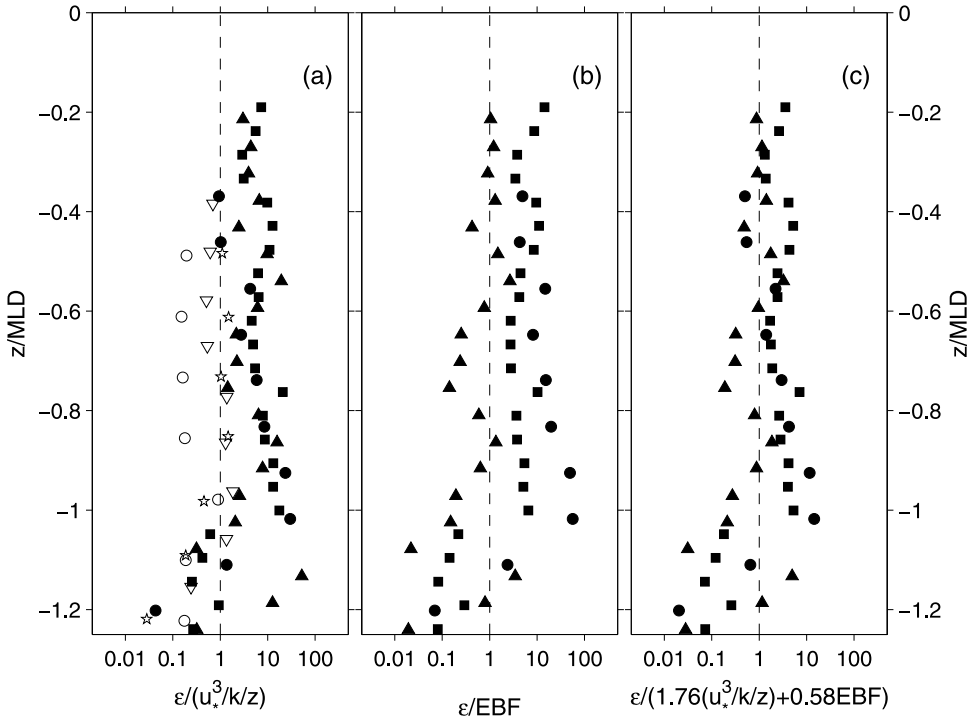

Figure 7. Scaling of mixed layer dissipation with (a) wind-scaling, $\epsilon_W = u_*^3/(\kappa z)$ for data during daytime ($u_* = \sqrt{\tau/\rho}$ is friction velocity, τ is wind stress estimated considering velocity difference between surface current and wind, κ is von Karman constant, and z is depth), (b) Ekman buoyancy flux (EBF), $b_y\tau_{DFW}/(\rho_o f)$ (b_y: meridional buoyancy gradient at the surface; τ_{DFW}: downfront wind stress; ρ_o: reference density; f: Coriolis parameter), and (c) with an empirical scaling using EBF, $\epsilon_{LG} = 1.76\epsilon_W + 0.58EBF$, plotted against nondimensional depth by mixed layer depth (<0.05°C from the surface). The abscissa is in log scale. Closed symbols are for dissipation data from mixed layer on the south side of the front, and open symbols are from north side. Markers are assigned for each station, as follows: open circles, 1; open triangles, 17; stars, 18; solid circles, 38; squares, 39; solid triangles, 40.

$/f = 21$ hours). Both the influence from local wind induced mixing and EBF due to downfront component are expected to contribute to the observed turbulence. The scaling when both wind and buoyancy flux contribute to mixing has been studied by *Lombardo and Gregg* [1989]. They found an empirical law, i.e., $\epsilon_{LG} = 1.76\epsilon_W + 0.58J_b^0$, where J_b^0 is positive buoyancy flux (cooling) at the surface. We employed this empirical form using EBF instead of J_b^0. The results of the scaling show that the observed dissipation rates are scaled better by the empirical law with EBF (Figure 7c). The ratios of mixed layer depth to Monin-Obkhov length based on EBF, $L = D/(u_*^3/\kappa EBF)$ for Stn. 38–40 are 0.52, 2.68, and 13.42, respectively. These ratios imply that mixed layer dissipation in Stn. 38 is controlled mainly by the wind (near surface data in Stn. 38, Figure 7a), whereas dissipation in Stn. 39–40 is influenced both by the wind and EBF (Figure 7c). The results show that scaled dissipation rates by EBF alone are still larger than unity by factor of 5–10 (Figure 7b). This suggests that the strong dissipation rates observed in the mixed layer front on the south side are caused by the local wind and EBF associated with the downfront wind.

[20] *Thomas et al.* [2008] showed that Ertel Potential Vorticity (PV) is reduced to near zero or even negative values due to frictional torque associated with downfront wind. We compute Ertel potential vorticity for a two-dimensional front, q_{N-S}, for each north–south section, including the 2008 data, assuming contributions from zonal gradients of density and velocity, and the contribution from vertical velocity are negligible, i.e.,

$$q_{N-S} = -\rho_o^{-1}\left[\left(f - \frac{\partial u}{\partial y}\right)\frac{\partial \sigma_\theta}{\partial z} + \frac{\partial u}{\partial z}\frac{\partial \sigma_\theta}{\partial y}\right], \qquad (2)$$

where y and z are meridional and vertical (positive upward) directions, u is zonal velocity, ρ_o is reference density, σ_θ is potential density minus 1000, f is Coriolis parameter. The q_{N-S} for the mixed layer in Leg A and E are computed using the surface current meter data, and surface temperature data averaged and recorded every 120 seconds, which allow resulting meridional density and velocity gradients to be of high spatial resolution. These surface data are averaged over 4 km horizontally and interpolated at each station. Since the density in the mixed layer on the south side of the Kuroshio Front is mostly determined by temperature (Figures 6a and 6e), we use objectively mapped salinity to compute surface density. Including salinity variations does not significantly alter the results. As LADCP data lacks near surface currents, meridional density gradient is used to estimate the background shear assuming thermal wind balance. The mixed layer averaged vertical density gradient, $\partial\sigma_\theta/\partial z$, is obtained for each station using CTD data. The 95% confidence interval for q_{N-S} at each station is computed as the maximum

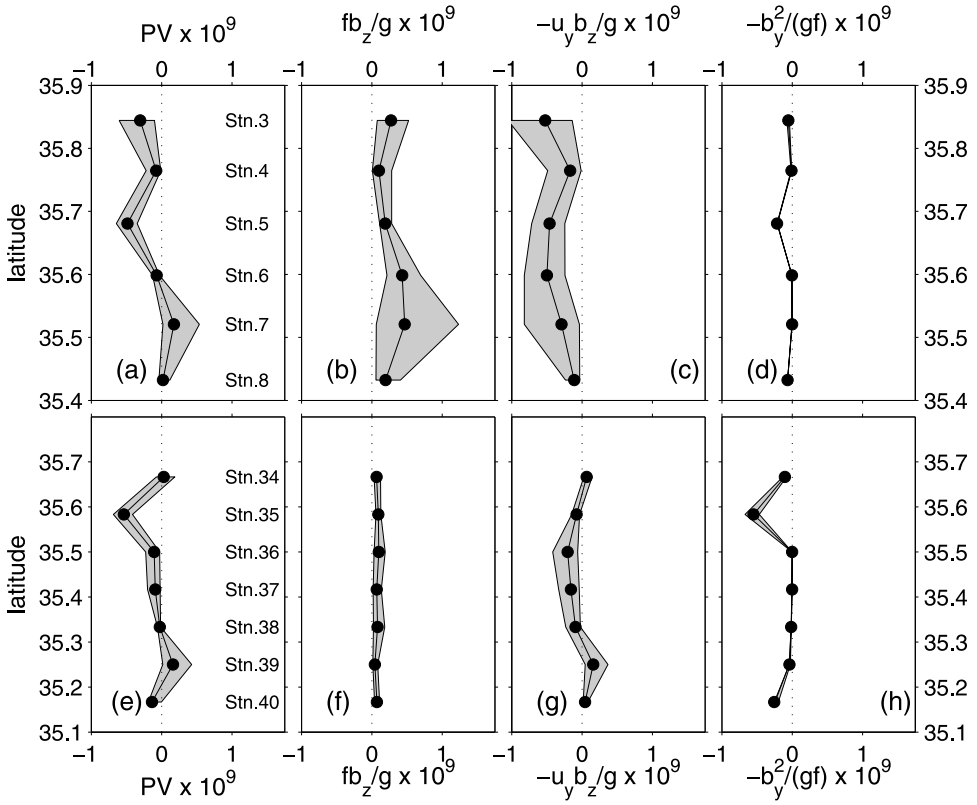

Figure 8. (a and e) Mixed layer q_{N-S} and its component for (b and f) planetary vorticity, $g^{-1}fb_z$, (c and g) tilting by vertical vorticity, $-u_y b_z g^{-1}$, and (d and h) tilting by horizontal vorticity, $g^{-1}u_z b_y$. Mixed layer q_{N-S} is obtained using surface current meter data, surface temperature records averaged every 120 seconds, and vertical density gradient at each station. These surface records are averaged every 4 km and interpolated at each station of Leg A and E. Objectively mapped salinity is used to compute surface density. The shading indicates 95% confidence intervals obtained by the bootstrap method with 5000 resamplings.

possible error band derived from the errors estimated for each component, such as the horizontal and vertical velocity and density gradients in (2). We use the bootstrap method with 5000 re-samplings at each averaging bin. The computed q_{N-S} using (2) on the south side of the Kuroshio Front for Leg A and E, shows that the mixed layer PVs exhibit negative signs (Figures 8a and 8e), which arise from vertical and horizontal tilting terms, $-u_y b_z g^{-1}$ and $-b_y^2 g^{-1} f^{-1}$, respectively, on the warm side of the front. We remind the reader that the symmetric instability criteria for two-dimensional front, $E^2N^2 < f^2M^2$ (where $E^2 = f(f - u_y)$, $N^2 = b_z$, $fM = b_y$, f is Coriolis parameter, and b is buoyancy) is identical to the condition that q_{N-S} is negative. The negative sign of q_{N-S} indicates that the mixed layer flow is symmetrically unstable. *Taylor and Ferrari* [2009] showed that such a situation leads to three-dimensional turbulence due to the secondary Kelvin-Helmholtz instability of the symmetrically unstable flow. As discussed in the next section, frictional reduction of PV is very efficient under the downfront wind conditions [*Thomas et al.*, 2008], which is observed during our experiments on the south side of the front. Note that at some stations, even $(f - u_y)b_z g^{-1}$ is negative, suggesting inertial instability. These conditions suggest that the directly observed elevated turbulent dissipation rates in the mixed layer on the warm side of the Kuroshio Front are influenced by inertial and/or symmetric instability [*Thomas and Lee*, 2005], similar to recent numerical [*Taylor and Ferrari*, 2009, 2010; *Thomas and Taylor*, 2010] and field studies [*Joyce et al.*, 2009; *D'Asaro et al.*, 2011].

3.2. Turbulence Near the Kuroshio Front Below the Mixed Layer

[21] Large microscale turbulent shear is observed in the tilted thermocline under the main Kuroshio Front at Stn. 5 in Leg A (Figure 6a) and Stn. 34 and 35 in Leg E (Figure 6e), similar to our 2008 Kuroshio observations [*Nagai et al.*, 2009] (also Figure 6f). These values of relatively strong turbulent shear are found to be equivalent to $\mathcal{O}(10^{-8} - 10^{-7})$ Wkg^{-1} of turbulent kinetic energy dissipation rate, ϵ. Including microstructure data measured in 2008, which shows ϵ, $\mathcal{O}(>10^{-7})$ Wkg^{-1} under the mainstream [*Nagai et al.*, 2009], it appears that the tilted thermocline under the deep Kuroshio mainstream is turbulent in both 2008 and 2009 observations, where the dissipation rate is one to two orders of magnitude larger compared to typical values found in open ocean thermocline. Recent microstructure observations in the Gulf Stream [*Winkel et al.*, 2002; *Inoue et al.*, 2010] also report much stronger turbulence in the thermocline, although these studies attribute the observed mixing in the thermocline entirely to internal

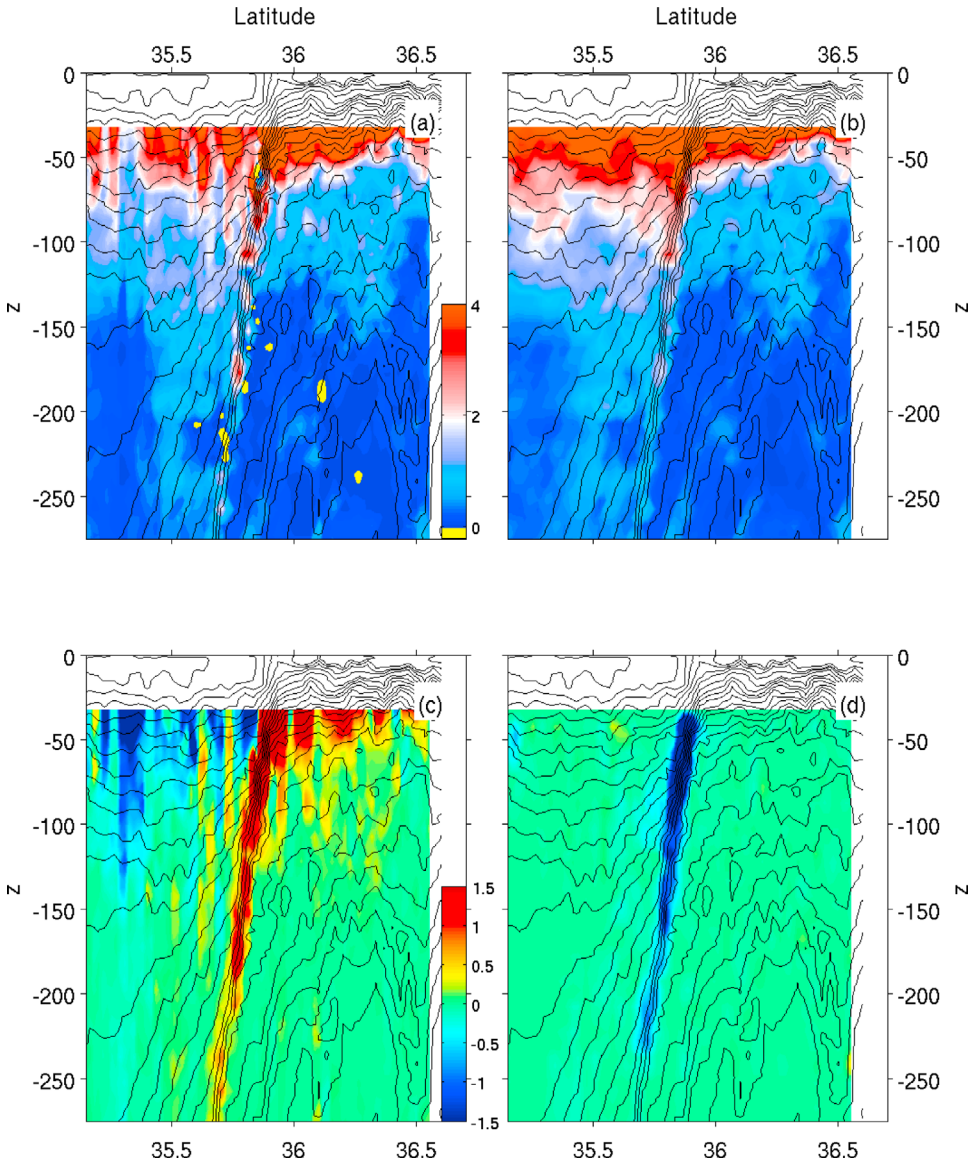

Figure 9. (a) Ertel Potential Vorticity for N–S transects, $q_{N-S} = g^{-1}[(f - u_y)b_z + u_z b_y]$(m^{-1} s^{-1}) for 2008 data. Density and ADCP zonal velocity are averaged over 4 km in the horizontal, and 16 m in the vertical. Density is derived from XBT observations every 3.7 km and CTD observations every 8.9 km across the Kuroshio Front. Shipboard ADCP data in 2008 are originally obtained averaging about every 300 m meridionally. Note that yellow indicates negative q_{N-S}. Also shown are each component of q_{N-S} for (b) planetary vorticity, $g^{-1}fb_z$, (c) tilting by vertical vorticity, $-u_y b_z g^{-1}$, and (d) tilting by horizontal vorticity, $g^{-1}u_z b_y$.

waves. Relatively large but somewhat patchy turbulent shear is also observed below 70 m, away from the tilted thermocline of the Kuroshio Front in Leg E and Leg A (Figures 6a and 6e).

[22] The vertical section of q_{N-S} and each vorticity component shown in Figure 9 are obtained by averaging the measured density and ADCP zonal velocity over 4 km in the horizontal and 16 m in the vertical. As horizontal resolutions of density and velocity measurements in 2009 data are rather coarse (9 km), the vertical section of q_{N-S} is shown only for the high-resolution data. However, the overall trend of PV distribution near the Kuroshio Front in 2009 is similar to that in 2008. An error analysis is performed for density and velocity using the bootstrap method with 1000 re-samplings for each grid point for 2008 data. Both the October 2009 (not shown) and the August 2008 data show large positive q_{N-S} along shallow thermocline (50–70 m) north of the Kuroshio Front, and in relatively deep thermocline (70–100 m) on the south side of the front, which may act as a barrier between low PV in the mixed layer and that in the interior of the Kuroshio region (Figure 9a). Low PV tendency is more evident at intermediate depth (>150 m), both on the north and south side of the Kuroshio Front. The low PV on the south side of the front is mainly due to the combination of anticyclonic vorticity contribution and weak stratification, $-u_y b_z/g$ (Figures 9b and 9c), whereas, on the north side the shear induced tilting term, $u_z b_y/g$, also plays an important

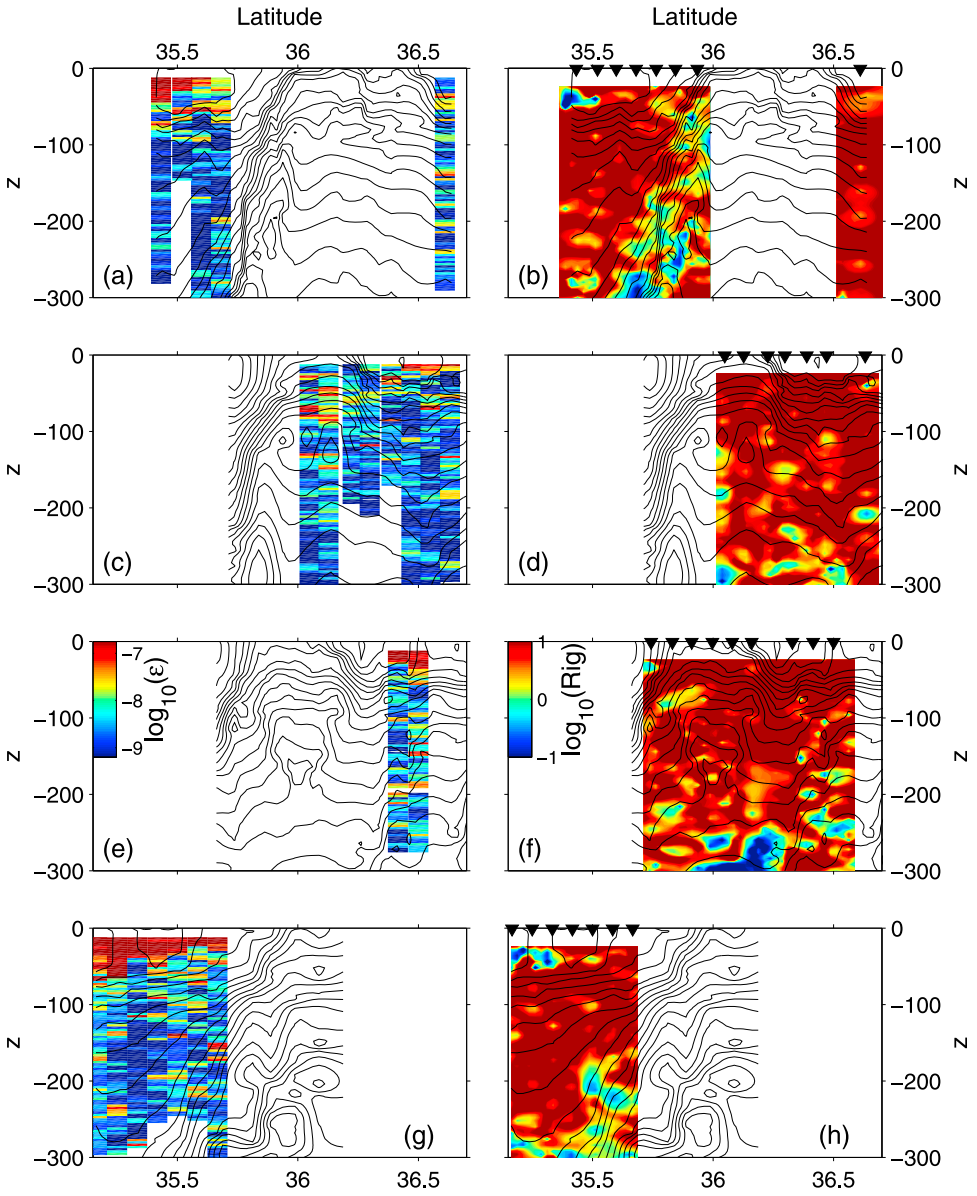

Figure 10. Turbulent kinetic energy dissipation rate obtained by integration of shear spectra for (a) Leg A, (c) Leg B, (e) Leg C, and (g) Leg E. Patterns of background Richardson number computed from mapped LADCP shear data and mapped potential density for (b) Leg A, (d) Leg B, (f) Leg C, and (h) Leg E.

role (Figures 9a, 9b and 9d). High PV water is found along the deep Kuroshio Front thermocline in Leg A for 2009 (not shown) and 2008 data (Figure 9a), similar to the low salinity tongue observed in Leg A (Figure 6a). However, the distribution of the high PV tongue is not as deep as low salinity subduction and becomes patchier at deeper depth. More importantly, the tongue of high PV water appears to be elongated toward the patches of negative q_{N-S} water distributed along the tilted thermocline of the Kuroshio Front (Figure 9a), marking the along isopycnal subduction of high PV in the tilted thermocline. The negative q_{N-S} region at 200–250 m depth is undergoing strong diapycnal mixing, as evidenced by the high dissipation rate (Figure 6f). A possible explanation is that the microscale turbulence is acting to reset the PV to zero. The negative q_{N-S} arises mainly from the shear tilting term, $u_z b_y/g$ (Figure 9d), which is extremely large for the 2008 data. The error analysis for q_{N-S} using the bootstrap method shows that the estimated upper bound of 95% confidence intervals are near-zero and remain negative in some portions near the front (Figure S2 in the auxiliary material). Along frontal gradients, which could arise from submesoscale flows and are neglected in (2), could contribute to the total PV. We estimate the contributions from the terms arising from these along frontal variations, such as $-v_z b_x/g$, $v_x b_z/g$, using surface temperature and salinity records and ship-board ADCP data at 224 m where the negative q_{N-S} is found (Figure 9a), measured while the ship was drifting eastward for the deployment of instruments. We use surface density to estimate zonal gradient because we do not have continuous density records at 224 m. The surface density gradient is an upper bound, as the buoyancy variation at the surface is expected to be larger than that at depth. The drifting occurred mostly in

zonal direction. The along frontal gradients are estimated over 4 km during the drifting to be consistent with the averaged distance for meridional gradients in (2). The meridional velocity varies little resulting only $\mathcal{O}(10^{-7}\mathrm{s}^{-1})$ of v_x over 4 km (Figure S3a in the auxiliary material). The vertical shear, v_z shows relatively weak value, $\mathcal{O}(10^{-3}\ \mathrm{s}^{-1})$ on average (Figure S3b in the auxiliary material). The meridional gradient of the surface buoyancy is estimated to be $\mathcal{O}(10^{-7}\ \mathrm{s}^{-2})$ (Figure S3c in the auxiliary material). These values lead to $\mathcal{O}(10^{-11})$ and $\mathcal{O}(10^{-12})\ \mathrm{m}^{-1}\ \mathrm{s}^{-1}$ for $-v_z b_x/g$ and $v_x b_z/g$, respectively. Based on the above error estimates, we conclude that grid averaged PV in the thermocline of the Kuroshio is near-zero. The strong turbulence found in the near-zero PV water suggests that the microscale turbulence may be resetting unresolved negative PV by undergoing symmetric instability as in *Taylor and Ferrari* [2009]. As *Haynes and McIntyre*'s [1987] impermeability theorem precludes generation of large volumes of net negative PV in the interior, the origin of the near-zero PV water in the thermocline is unclear, though there are two possibilities. One possibility for its origin is the interaction of the Kuroshio with the Izu-Ogasawara ridge, which is 200–300 kilometers upstream from the observation site. (For example, density surface of $\sigma_\theta = 26$ is as shallow as 200 m under the Kuroshio mainstream, but as deep as 500 m on the south side of the front). Since the Kuroshio, whose frontal signature is deeper than 500 m, mostly passes through the ridge, which includes a large area of shallow regions (<500 m) and several islands (Figure 3a), it is possible that the low PV water is created by intense mixing at the bottom boundary or sidewall of the ridge [e.g., *Hasegawa et al.*, 2004], and, transported or upwelled along isopycnal to the observation site within a few days. Argo float profiling data in Nov. 2009 show that the deepest potential density reaches $\sigma_\theta = 26 - 26.5$ just above the bottom (Figure S4 in the auxiliary material). This suggests that the near-zero PV water of $\sigma_\theta = 26 - 26.5$ found under the Kuroshio with strong turbulent dissipation, could have been transported along isopycnals after the formation at the ridge. Another possibility is the formation of the negative PV at the surface upstream of the Kuroshio, which is subducted and isolated from the surface by advective processes [*Thomas*, 2008]. In 2008, there were no significant wind events in the month preceding the observations [*Nagai et al.*, 2009], whereas in 2009, there was a typhoon a week before the observations.

[23] Direct observation of microscale turbulence under the Kuroshio shows intense turbulence in the same region (Figure 6f) and in the same depth range of 200–300 m where patchy negative q_{N-S} values are found in the 2008 data (Figure 9a). These conditions in our observations at depth are in contrast to the near surface forced symmetric instability driven by downfront wind in the subpolar front of Japan/East Sea [*Thomas and Lee*, 2005], the Gulf Stream [*Joyce et al.*, 2009], and the Kuroshio (Figure 9e) [*D'Asaro et al.*, 2011], where the near surface negative PV water is formed through positive buoyancy flux [*Taylor and Ferrari*, 2010] and frictional reduction due to downfront wind, extracting high PV from the base of the mixed layer [*Thomas*, 2005]. In the sections presented here, a vast reservoir of the low PV water is present below the thermocline, that turns out to be near-zero in patches under the Kuroshio mainstream. The low PV characteristics found on the south side of the Kuroshio Front correspond to Subtropical Mode Water (STMW) in western North Pacific (~400 m depth), which is believed to be formed through wind and convective mixing in winter [*Qiu and Chen*, 2006]. On the other hand, the low PV north of the Kuroshio could be influenced from low PV and salinity characteristics of Oyashio water [*Yasuda*, 2004].

[24] Although the strong and deep jet of the Kuroshio surrounded by the low PV water at intermediate depth (>150 m) is preconditioned for symmetric instability, sign reversal in PV is a necessary condition for onset of instability. Here, we examine the rate at which the internal mixing and friction can modify the near-zero or negative PV. The rate of change in the Ertel PV, q, due to diabatic processes can be written [e.g., *Marshall and Nurser*, 1992; *Thomas et al.*, 2008] as follows,

$$\frac{Dq}{Dt} = -\frac{\nabla}{g}\cdot\left(\nabla b \times \mathbf{F} - \frac{Db}{Dt}\omega_{\mathbf{a}}\right), \tag{3}$$

where g is gravitational acceleration, b is buoyancy, $\mathbf{F}$ is frictional force vector, and $\omega_{\mathbf{a}}$ is absolute vorticity.

[25] As *Thomas et al.* [2008] review, atmospheric buoyancy forcing and wind stress, acting on the surface of the front can induce non-advective PV flux, $\mathcal{J}$, through $\mathcal{D}$ and F, respectively, i.e.,

$$\mathcal{J} = \frac{1}{g}\left[\left(f - \frac{\partial u}{\partial y}\right)\mathcal{D} + \frac{\partial b}{\partial y}F\right]\Big|_{z=0}, \tag{4}$$

for two-dimensional front with constant shear and stratification, where $\mathcal{D} = Db/Dt$ and F is the divergence of vertical momentum flux at the surface.

[26] The first term of (4) can be negative when positive buoyancy flux (cooling) is forced at the surface ($\mathcal{D} = Db/Dt < 0$) with positive absolute vertical vorticity ($f - u_y > 0$), and the second term becomes negative when downfront wind stress ($F > 0$ for eastward flowing frontal jet consistent with $b_y < 0$), effectively reduces the PV.

[27] For the 2009 observations, an order of magnitude estimate for the nighttime surface positive buoyancy flux (cooling), J_b^0 at $z = 0$, is $10^{-7}\ \mathrm{Wkg}^{-1}$, and momentum flux, τ / ρ is $10^{-4}\ \mathrm{m}^2\ \mathrm{s}^{-2}$. These values, with $b_y \sim \mathcal{O}(10^{-6}\ \mathrm{s}^{-2})$ and $f - u_y \sim \mathcal{O}(10^{-4}\ \mathrm{s}^{-1})$ lead to the ratio of the first term to the second term in bracket of (4) to be 0.1, suggesting that the momentum flux at the surface is the dominant contributor to PV flux in 2009. For the 2008 observations, because wind was weak, <5 ms^{-1}, both buoyancy and momentum flux are expected to be important contributors to PV flux during nighttime. Although we do not have shortwave radiation data, we expect stabilization during the day with negative buoyancy flux (solar heating) playing a role in suppressing the instability more strongly during 2008 than 2009.

[28] Near the Kuroshio Front, patchy turbulence is observed in the region where $q_{N-S} < 0$ (isopycnal tilt becomes steeper than that of isoline of the absolute momentum). This implies that symmetric instability and subsequent K-H instability along tilted isopycnal [*Taylor and Ferrari*, 2009] may be active in this region. Strong turbulent dissipation, $\mathcal{O}(10^{-7}\ \mathrm{Wkg}^{-1})$, observed in the tilted thermocline with $N^2 \sim \mathcal{O}(10^{-4}\ \mathrm{s}^{-2})$ in the near-zero PV water in 2008 corresponds to a large value for *Turbulent Activity*, $\epsilon/(\nu N^2) \sim \mathcal{O}(10^3)$, where ν is kinematic molecular

viscosity, suggesting that the flow is undergoing three-dimensional isotropic turbulent mixing with $\mathcal{O}(1)$ Richardson number. Under such conditions, turbulent Prandtl number, $Pr = A_v/K_v \sim 1$, and turbulent diffusion fluxes of momentum and buoyancy for the mean state may be represented with eddy diffusivities, which are estimated from measured dissipation rates (5). Accordingly, rate of change of the mean PV caused by turbulent processes for two-dimensional front with non-constant shear and stratification may be written as follows, $g^{-1}\partial_y[u_z\partial_z(K_z b_z) - b_z\partial_z(A_v u_z)] + g^{-1}\partial_z[(f - u_y)\partial_z(K_z b_z) + b_y\partial_z(A_v u_z)]$. This equation can be scaled as $f_o S^2 A_o/\delta z^2$ for the first, second, and fourth term, and $f_o N^2 A_o/\delta z^2$ for the third term, scaling b_z by $N^2 \sim \mathcal{O}(10^{-4}\ \mathrm{s}^{-2})$, u_z by $S \sim \mathcal{O}(10^{-2}\ \mathrm{s}^{-1})$, b_y by $fS \sim \mathcal{O}(10^{-6}\ \mathrm{s}^{-2})$ (Thermal-wind), $f - u_y$ by $f_o \sim \mathcal{O}(10^{-4}\ \mathrm{s}^{-1})$, $A_v \sim K_z$ by $A_o \sim \mathcal{O}(10^{-4} - 10^{-3}\ \mathrm{m}^2\ \mathrm{s}^{-1})$ as in the observations, ∂_z by $1/\delta z \sim \mathcal{O}(10^{-2}\ \mathrm{m}^{-1})$ (representing the shear layer thickness as 100 m), ∂y by $(fS\partial z)/N^2 \sim \mathcal{O}(10^{-4}\ \mathrm{m}^{-1})$ (using b_y/N^2). For all the terms, this leads to $\mathcal{O}\left(10^{-17} - 10^{-16}\right)\ \mathrm{m}^{-1}\ \mathrm{s}^{-2}$, depending on the magnitude chosen for A_o. The rate of change in PV of $\mathcal{O}\left(10^{-17} - 10^{-16}\right)\ \mathrm{m}^{-1}\ \mathrm{s}^{-2}$ suggests that it requires $\mathcal{O}$(1–10) days to alter the PV as much as $\mathcal{O}\left(10^{-11}\right)\ \mathrm{m}^{-1}\ \mathrm{s}^{-1}$ due to vertical turbulent friction and mixing alone. Since the negative PV water created at the bottom boundary of the Izu-Ogasawara ridge would arrive at the observation site in approximately 2–3 days, bottom/side-wall boundary is one possible source of the negative PV in the thermocline. This topographic origin is in contrast to the previous observational [*D'Asaro et al.*, 2011] and theoretical studies [*Thomas and Lee*, 2005; *Thomas and Taylor*, 2010] where symmetrically unstable condition arises by the surface boundary, which is balanced by extracting high PV water from below the surface mixed layer.

[29] The criterion of symmetric instability for a two-dimensional front can be rewritten with nondimensional parameters, gradient Richardson number, $Ri_g = N^2/S^2$, and Rossby number, $Ro = -f^{-1}u_y$, i.e., $(1 + Ro)Ri_g < 1$. In the mixed layer on the south side of the front in Leg E where intense turbulence is observed, q_{N-S} includes negative values (Figure 9e), i.e., $(1 + Ro)Ri_g < 1$, because of the anticyclonic vorticity ($Ro < 0$) with small Ri_g. However, the region under the Kuroshio main axis (~230 m) on the cyclonic side of the front ($Ro > 0$, Figure 12h) where strong turbulence is observed in 2008 (Figure 6f), is found to be neutral with respect to the criterion for symmetric instability (Figure 9a) as the very sharp front corresponds to very small values of Ri_g (Figure 10), even though the large positive Rossby number ($Ro > 0$) opposes the tendency of the small Ri_g to lower $(1 + Ro)Ri_g$ less than unity. Background gradient Richardson number, Ri_g, shows $\mathcal{O}(1)$ or smaller values along tilted thermocline of the Kuroshio Front in Leg A, and E as shown in previous observations [*Nagai et al.*, 2009] where observed turbulent dissipation rates are relatively large. However, for many locations, relatively large dissipation rates are not associated with low background Ri_g (Figure 10). Turbulence driven by interactions of internal waves has been parameterized empirically with weaker dependency on the background Ri_g [*Gregg*, 1989; *MacKinnon and Gregg*, 2003]. Therefore, the turbulence in relatively large $Ri_g > 1$ regions may indicate the influence of internal waves. Recent field studies have observed coherent bands of shear, which are considered to be near-inertial waves, under the Gulf Stream [*Inoue et al.*, 2010], near the Japan/East Sea Subpolar Front [*Shcherbina et al.*, 2003], and between shelf and the Kuroshio Front [*Rainville and Pinkel*, 2004]. Although our velocity measurements by LADCP are spatially rather coarse in horizontal direction, shear square, $S^2 = u_z^2 + v_z^2$ shows coherent bands in several locations in observed transects (Figure 11). In Leg A, large S^2 is found along tilted thermocline of the Kuroshio Front, forming bands of S^2 in the 100–200 m depth range, and along shallow thermocline around 50–100 m depth range (Figure 11a). Similar to Leg A, in leg E large S^2 is found along shallow and deep thermocline of the Kuroshio Front (Figure 11i). Although patchier than leg A and E, coherent shear bands are also observed north of the Kuroshio Front in Leg B, C, and D (Figures 11c, 11e, and 11g). As these observations are near the front, geostrophic shear is expected to dominate. Computed geostrophic shear square, $(f^{-1}\,\partial b/\partial y)^2$, is found to be in agreement with observed S^2 pattern especially near the Kuroshio Front. Banded structures in geostrophic shear associated with cold water tongue are seen in Leg A under the Kuroshio mainstream below 200 m, similar to the observed S^2 (Figures 11a and 11b). This result indicates that the observed shear is mainly dominated by geostrophic shear, except for S^2 north of the front and along shallow thermocline south of the front in Leg E.

[30] The velocity vectors turn with depth for vertically propagating near-inertial waves [*Shcherbina et al.*, 2003]. Differences in velocity variance between clockwise (downward energy propagation) and anti-clockwise (upward energy propagation) turning components are estimated using rotary wave number spectra computed for LADCP data in 2009 surveys and shipboard ADCP data in 2008 (Figure 12). Vertical wave number auto-spectra and co-spectra of u and v are computed using modified periodogram method with a cosine window to obtain the rotary spectra. These results show that the clockwise velocity variance is dominant on the south side of Leg E (Figure 12e), which corresponds to downward propagation of internal waves. Normalized effective Coriolis parameter, $f_{eff}^{o} = f^{-1}\sqrt{f^2 - fu_y}$, computed using LADCP and ADCP data suggest that anticyclonic side of the front could potentially trap the near-inertial waves (Figures 12c and 12g). The turning of the shear, represented by $-\tan^{-1}(V_z/U_z)_z$, is very limited in the tilted thermocline of the sharp front in Leg A from 50 through 300 m, where Ri_g is $\mathcal{O}(1)$ or smaller (Figure S5 in the auxiliary material). The ADCP data in the extremely sharp Kuroshio Front observed in 2008 also shows that shear turning with depth is small along the tilted thermocline of the front where Ri_g is $\mathcal{O}(1)$ or smaller (Figure S5f in the auxiliary material). This result indicates that the shear at the sharp front is dominated by thermal-wind shear of the Kuroshio jet.

3.3. Statistics of Microstructure Data and Implications for Hydrography Near the Kuroshio Front

[31] Observed turbulent dissipation rates, ϵ in 2008 and 2009, averaged into binned log space of N^2 and S^2 show that relatively large ϵ can be categorized into two groups, i.e., Group One in low $Ri_g < \mathrm{O}(1)$ region and Group Two in large

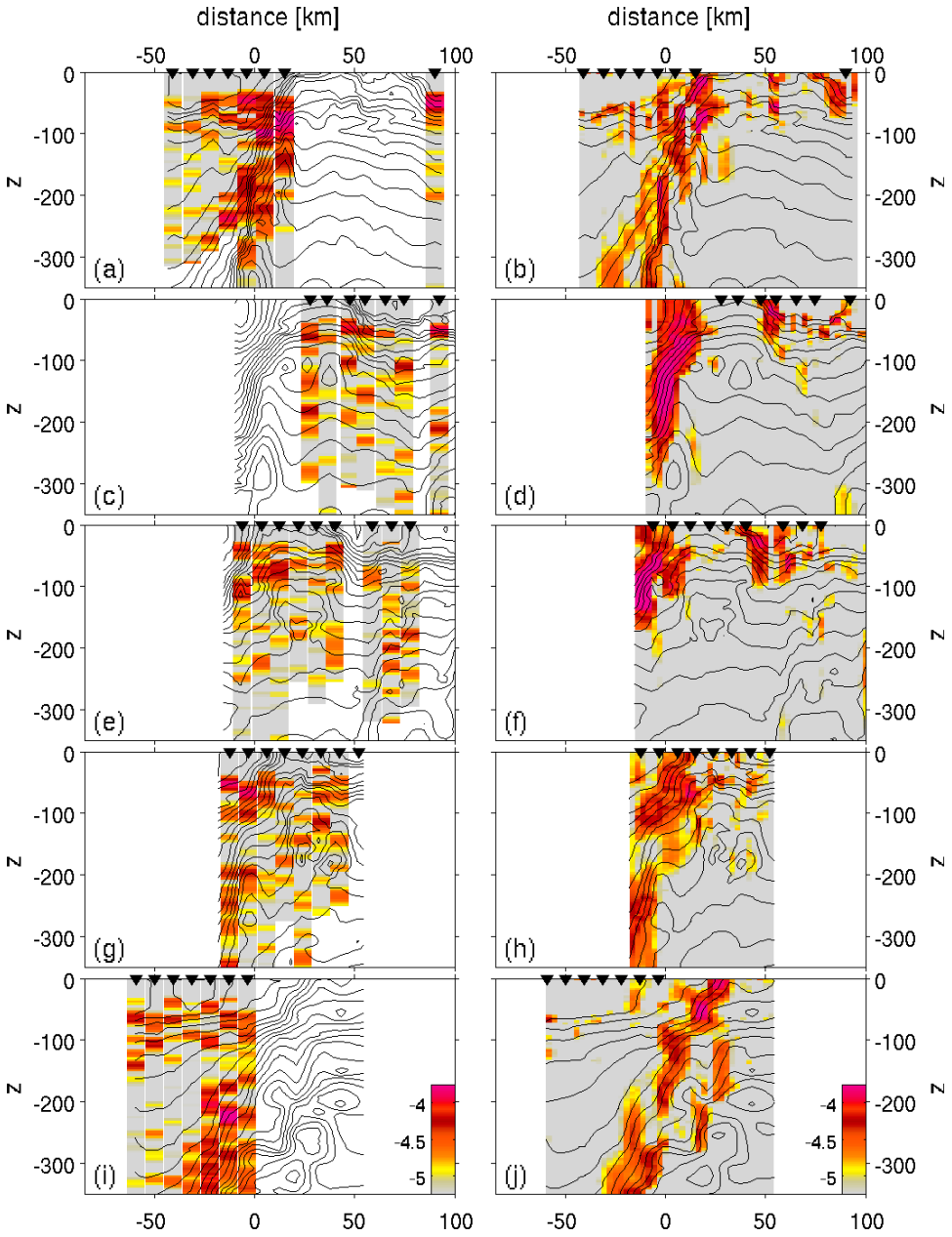

Figure 11. Comparison between (left) observed squared shear and (right) equivalent counterpart of geostrophic shear, $(-f^{-1}b_y)^2$ for (a, b) Leg A, (c, d) Leg B, (e, f) Leg C, (g, h) Leg D and (i, j) Leg E (s^{-2}).

N^2 (Figure 13b). The first group occurs in relatively deeper layer (150–200 m) with some exceptions in well mixed near surface waters, whereas the second group is found in relatively shallow layer (50–150 m Figure 13d). The former group mostly consists of relatively large ϵ found with low Ri_g at the Kuroshio Front thermocline, and the latter corresponds to that observed with relatively large $Ri_g > 1$, e.g. in upper 150 m of Leg E and B (Figure 10). Both groups occur at relatively large horizontal buoyancy gradients (Figure 13c), suggesting that it is near the front that statistically rare and high dissipation occurs (Figures 13a, 13b, and 13c).

[32] The second group with large ϵ and large N^2 resembles a recent internal wave empirical parameterization by *MacKinnon and Gregg* [2003] (hereinafter, MG-scaling), who found better agreement between observed ϵ and predicted ones in a shelf sea, with an assumption that large-scale background internal wave shear comes primarily from low frequency waves, which may also be relevant for upper ocean frontal regions. Comparisons between observed dissipation rates and MG-scaling shows significant but weak positive correlation (Figure S6 in the auxiliary material, $R = 0.24$, significant with 99% confidence interval).

[33] The two distinct groups of ϵ observed here for very different values of Ri_g, which is a dynamically important nondimensional parameter, implies that the single parameterization for internal waves may not be appropriate for these observations. The large ϵ in the first group may be associated

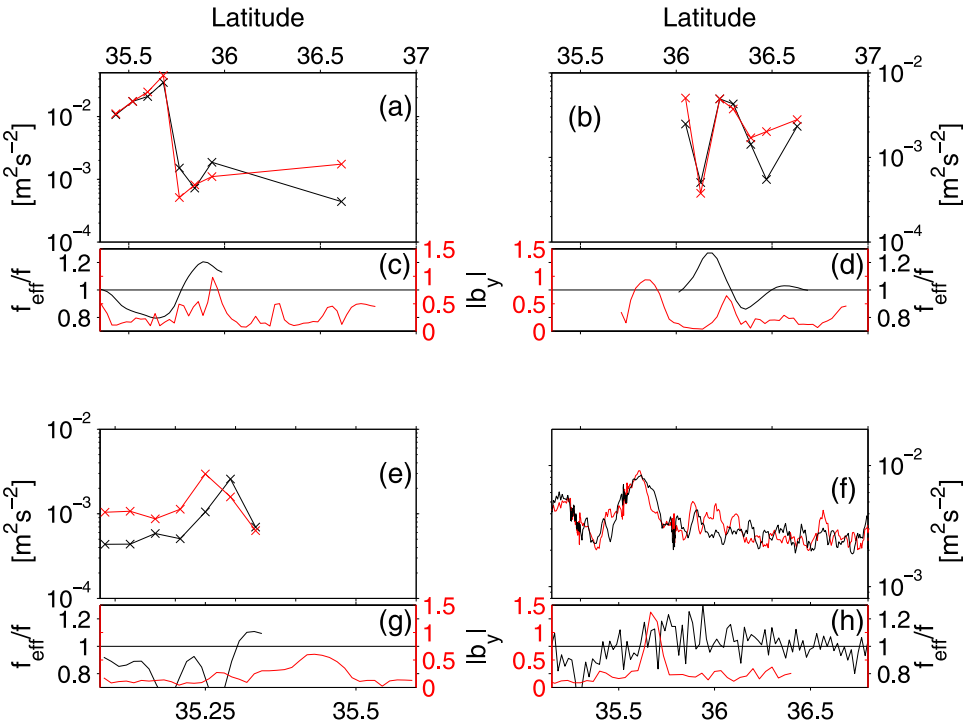

Figure 12. (a, b, e, f) Rotary spectra of velocity integrated along vertical wave number for (red) clockwise (downward energy propagation) and (black) anti-clockwise (upward energy propagation) components ($m^2\ s^{-2}$). (c, d, g, h) Effective Coriolis parameter shown in solid black lines normalized by local Coriolis parameter ($f^{-1}\sqrt{f^2 - fu_y}$) averaged over 300 m depth for Leg A (Figures 12a and 12c), Leg B (Figures 12b and 12d), and Leg E (Figures 12e and 12g) and 2008 data (Figures 12f and 12h). In Figures 12c, 12d, 12g, and 12h, the solid red lines show surface meridional buoyancy gradient ($10^{-6}\ s^{-1}$) to represent the location of the front. The integrated rotary spectra for 2008 surveys in Figure 12f are moving-averaged along meridional direction over 3 km.

with direct dissipation at the front [*McWilliams et al.*, 2009; *Molemaker et al.*, 2010; *Capet et al.*, 2008a, 2008b, 2008c] while in the second group it may be associated with internal wave breaking [*Inoue et al.*, 2010; *Winkel et al.*, 2002], irrespective of whether the internal waves origin is remote or generated at the front [*Plougonven and Snyder*, 2007].

[34] The strong turbulence observed near the low salinity tongue at Stn. 5 in Leg A and in the halocline in Leg B, and C (Figure 6) suggest that low salinity water could be mixed diapycnally with the saltier Kuroshio water near the front, contributing to formation of intermediate water masses, such as the North Pacific Intermediate Water (NPIW) [*Yasuda*, 2004]. The NPIW, which is distributed over the entire subtropical gyre of the North Pacific, is characterized as the salinity minima between 300 and 800 m depth, associated with a pycnostad between 26.6 and 27.2, which do not outcrop in open water of entire North Pacific. $\theta - S$ diagrams with turbulence data show that relatively strong dissipation rates $\mathcal{O}(10^{-8} - 10^{-7})$ Wkg^{-1} are found between the Kuroshio water and water influenced by the Oyashio in the Kuroshio-Oyashio Mixed Water region at 60–250 m depth, reaching the periphery of the NPIW pycnostad, σ_θ = 26.6 (Figures 14a and 14b).

[35] The eddy diffusivity for our profiles is estimated using observed dissipation rate and stratification [*Osborn*, 1980], i.e.,

$$K_\rho = \frac{0.2\epsilon}{N^2}. \tag{5}$$

The range of computed eddy diffusivity is found to be $\mathcal{O}(10^{-5} - 10^{-3})$ $m^2\ s^{-1}$, and reaches $\mathcal{O}(10^{-4} - 10^{-3})$ $m^2\ s^{-1}$ at 100–300 m depth on average. These are one to two orders of magnitudes larger than typical thermocline values (Figure 14d). This suggests that diapycnal mixing in the halocline near the Kuroshio Front can diffuse the low salinity water. Concurrently, the mesoscale confluence can bring the low salinity to layers above and below (see section 4). Therefore, these two processes acting in tandem can contribute to the net ventilation of the low salinity water. $\theta - S$ diagram with averaged depth indicates such along isopycnal subduction (or isopycnal mixing) can also be ventilation in physical space (e.g. pycnostad 26–27 in Figure 14c). Potential vorticity, q_{N-S} shows along and cross isopycnal variation and indicates that relatively low PV water appears in deeper layer (>150 m) on both sides of the Kuroshio Front, as well as in the surface mixed layer on the south

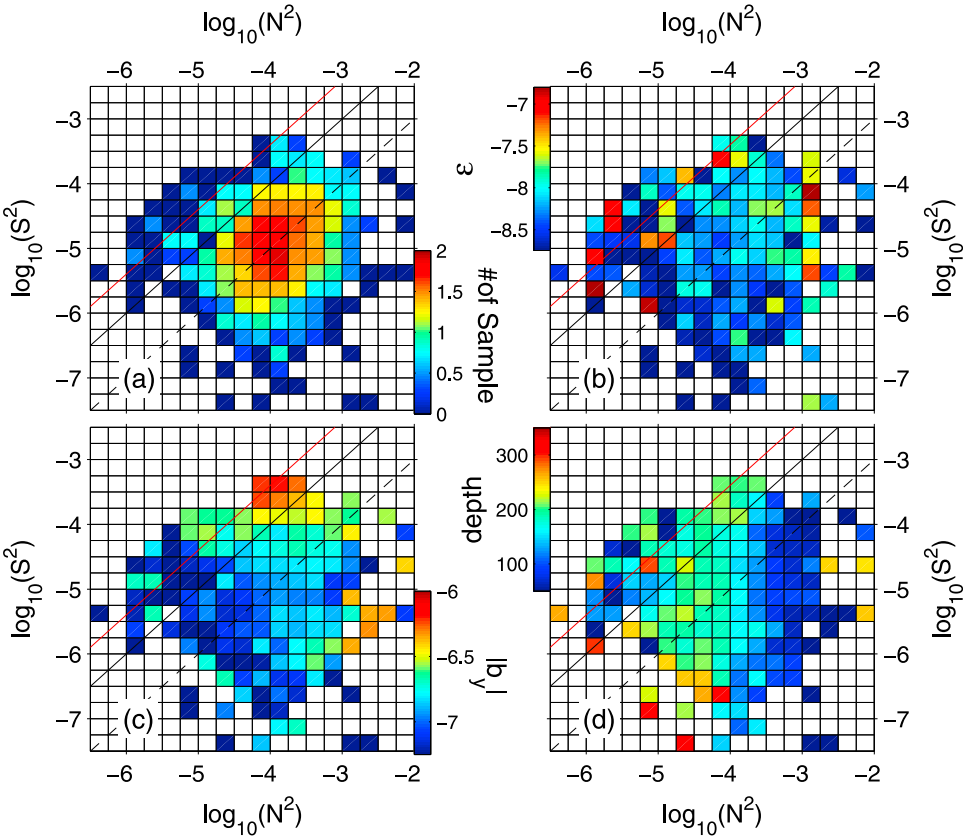

Figure 13. (a) Log of number of samples of measured turbulent kinetic energy dissipation rate averaged in bins of log of squared buoyancy frequency, N^2 and shear square, S^2. (b) Same as Figure 13a but for log of measured turbulent kinetic energy dissipation rate $\log_{10}(\mathrm{Wkg}^{-1})$. (c) For log of meridional buoyancy gradient $\log_{10}(s^{-2})$. (d) For depth of sample (m). Solid lines indicate gradient Richardson number, Ri_g = 0.25 (red) and 1 (black). Broken line indicates Ri_g = 10.

side of the front, and are consistent with the positions of relatively large K_ρ in $\theta - S$ space. The cold tongue emanating from below and low salinity tongue emanating from above in physical space can be seen as zigzag $\theta - S$ lines in between two dominant groups of water masses across the Kuroshio Front (Figure 14c). The turbulent mixing between these water masses across the front found in $\theta - S$ diagram suggests that the observed tongue or mound like thermohaline structures are highly diabatic.

4. Mesoscale Forcing and Subduction and Upwelling

[36] Observed temperature and salinity data are mapped horizontally with two exponentially decaying covariance models, $exp(-\mathbf{r}/\sigma_\mathbf{r})$, which are functions of zonal and meridional distance, $\mathbf{r}$, and decorrelation length scales for each direction, $\sigma_\mathbf{r}$, respectively. The decorrelation length scales obtained by least squares fit of covariances to the models are 122 km and 34 km for zonal and meridional directions, respectively. The monthly mean climatology of World Ocean Atlas 2005 (WOA05) are interpolated at the depths of horizontal maps, and utilized to construct mean temperature and salinity fields.

[37] The domain of the three-dimensional map is expanded to a 470 km × 550 km × 1000 m box to avoid strong boundary effects onto the interior solution. As our XBT temperature measurements are limited at most to 750 m depth, the density structure below 750 m is linearly relaxed to the horizontally uniform density field at the bottom. Nondivergent geostrophic flow is obtained by solving an elliptic equation for the geostrophic stream function ($\psi_x = v_g$, $\psi_y = -u_g$) as in *Rudnick* [1996]. As our velocity data are limited to the upper 300 m at most of CTD/LADCP stations, the geostrophic stream function and associated **Q** vector below 300 m are based only on the density field, while they are obtained both from measured horizontal flow field and density field in upper 300 m. In the limit of adiabatic flow and small Rossby number, the vertical velocity has been traditionally inferred using Quasigeostrophic- ω (QG-ω) equation, i.e.,

$$\nabla_h^2(N^2 w) + f^2 \frac{\partial^2 w}{\partial z^2} = 2\nabla_h \cdot \mathbf{Q}, \tag{6}$$

where $\nabla_\mathbf{h}$ is horizontal derivative operator, and **Q** is the so-called **Q** vector, defined as $(\psi_{xy} b_x - \psi_{xx} b_y, \psi_{yy} b_x - \psi_{xy} b_y)$. The frontogenesis function defined as a product of **Q** and $\nabla_\mathbf{h} b$ normalized by $|\nabla_\mathbf{h} b|$, i.e.,

$$\frac{D|\nabla_\mathbf{h} b|}{Dt} = \frac{\mathbf{Q} \cdot \nabla_\mathbf{h} b}{|\nabla_\mathbf{h} b|}, \tag{7}$$

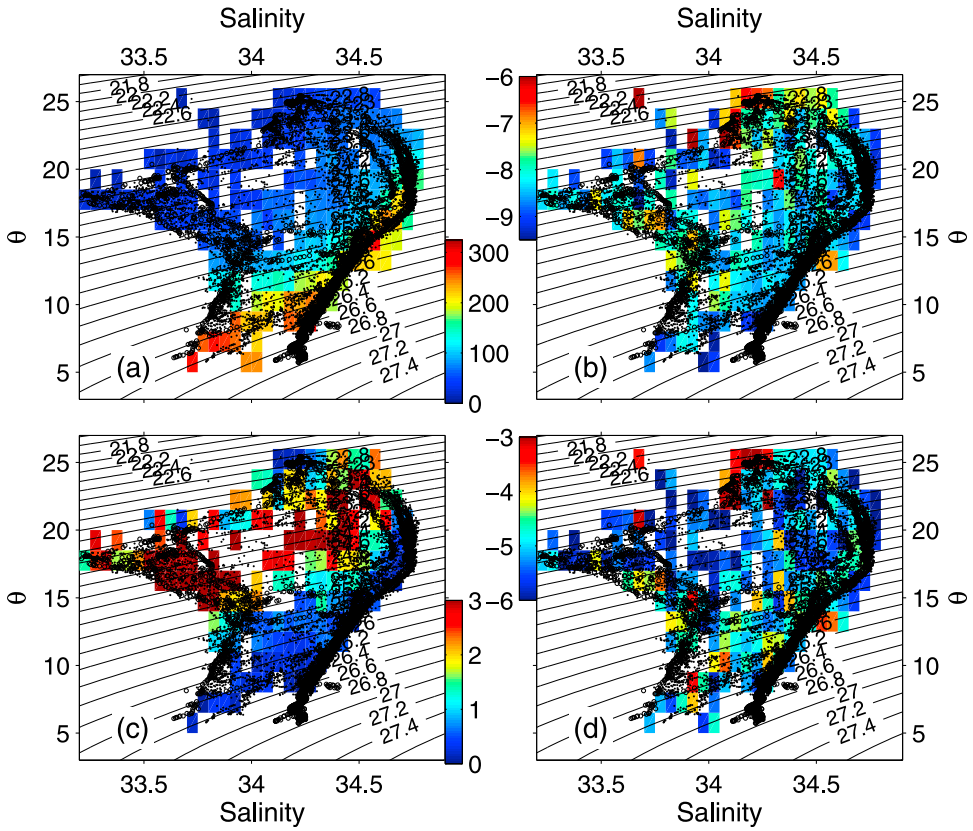

Figure 14. $\theta - S$ diagram from (dot) CTD observations and (circle) Underway CTD observations. Color indicates (a) depth of TurboMAP sample (m), (b) log of turbulent dissipation rate $\log_{10}(\mathrm{Wkg}^{-1})$, (c) log of PV_{N-S} $\log_{10}(\mathrm{m}^{-1}\ \mathrm{s}^{-1})$, and (d) log of K_{ρ} $\log_{10}(\mathrm{m}^{-2}\ \mathrm{s}^{-1})$.

is also the Lagrangian rate of change of buoyancy gradient. The sign of this function determines whether the front is under frontogentic condition ((7) > 0), or frontolytic condition ((7) < 0) [*Bluestein*, 1993]. Equation (6) is discretized using finite difference with horizontal and vertical resolutions of 1/40° and 4 m, respectively, and solved for the vertical velocity, w, with zero boundary condition at all boundaries. The domain ranges from 142°E through 147°E zonally, 33.5°N through 38.5°E meridionally and 0 through 1000 m vertically. Although the mainstream of the Kuroshio Front is hardly characterized as a small Rossby number flow, a higher order balanced model, such as the Semigeostrophic equation breaks down because of the sign reversal of the PV. Therefore, (6) is solved only to provide rough patterns of up- and downwelling rather than accurate values of the vertical velocity.

[38] The solution for the frontogenesis function shows alternating signs along the weakly meandering Kuroshio Front (Figures 15a and 15b). Frontogenesis ((7) > 0) appears in Leg A through C, where the mesoscale meander changes from crest to trough and frontolysis ((7) < 0) is found in Leg D through E, where the mesoscale meander changes from trough to crest (Figure 15). However, it is not constant with depth, and two different signs can appear along the same north–south transect (Figure 16). For Leg A, frontogenetic tendency dominates at the center of the Kuroshio Front and frontolytic tendency is also seen in the upper 150 m on the north side of the Kuroshio Front (Figure 16a). In contrast, for Leg D and E, frontolytic tendency dominates at the center of the front and frontogenetic tendency is found in the upper layers on the north side (Figures 16c and 16e). This pattern of frontogenesis at the center of the front with frontolysis to the north in the meander crest to trough region and vice versa for the meander trough to crest region are consistent with the results of neutral buoy experiments shown in Figure 14 of *Bower* [1989]. The inferred vertical velocity shows alternating up- and downwelling with magnitude exceeding $\mathcal{O}(10\ \mathrm{mday}^{-1})$, which are confined to the frontal region (Figures 15c and 15d). Although the three-dimensional solution of (6) allows dominance of single sign of either downwelling or upwelling at a cross frontal section, which differs from that of the two-dimensional picture, the overall pattern shows downwelling on the dense side and upwelling on the less dense side of the front in frontogenetic condition and vice versa for frontolysis (Figure 15).

[39] For Leg A where the frontogenesis dominates at the center of the front, downwelling and upwelling over 20 mday^{-1} are inferred on the north side and from the center to the south side of the Kuroshio Front, respectively (Figure 16). The downwelling for Leg A is consistent with the low salinity tongue extending from the surface to over 300 m depth and could explain its formation on the north side of the front (Figure 6a). On the other hand, the upwelling inferred at the center of the front is consistent with observed cold water tongue extending from lower layer in Leg A (Figure 16b). The central upwelling at the mixed layer

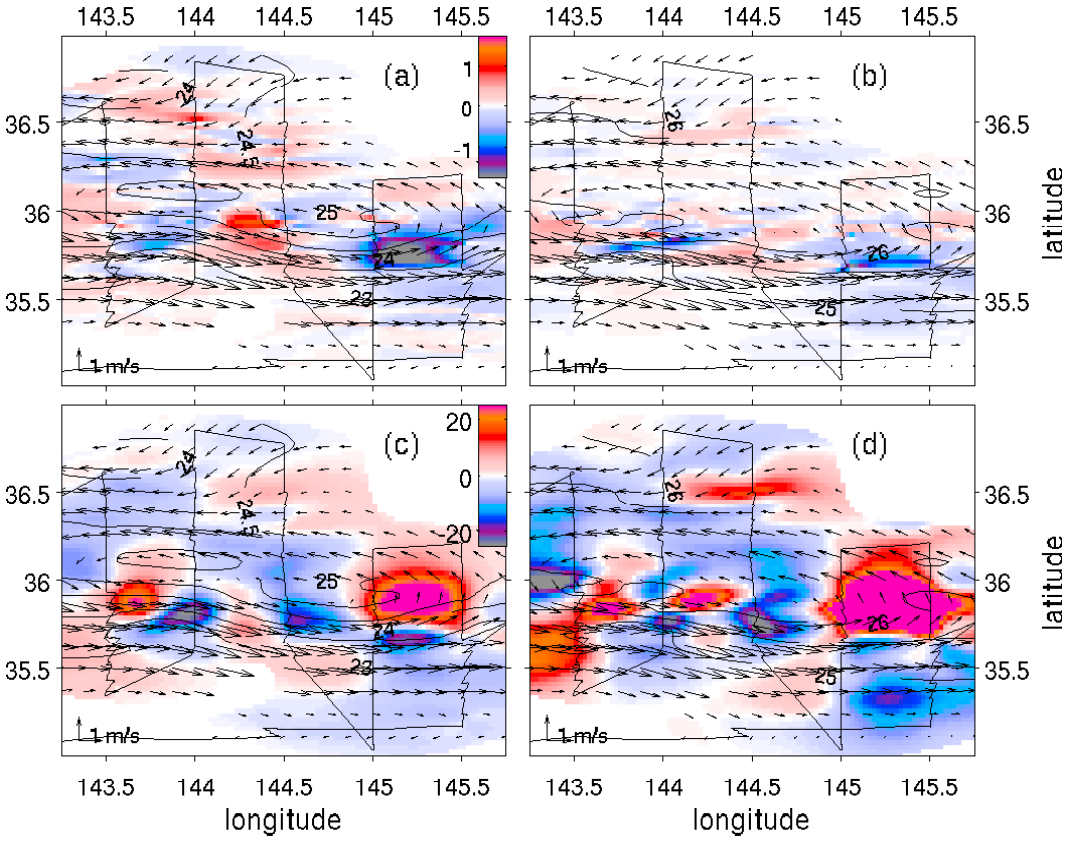

Figure 15. Horizontal section of (top) frontogenesis function equation (7) $\times 10^{11}$ s^{-3} and (bottom) vertical velocity ($mday^{-1}$) inverted using (6) at (a, c) 50 m depth and (b, d) 150 m depth. Black contours show horizontal section of mapped density. Vectors show mapped nondivergent geostrophic flow field. Only region where noise variance is less than 8% of the total is shown.

front in the upper 100 m of Leg A (Figure 16b) is a continuation of deep mesoscale upwelling. The horizontal structure of this upwelling is confined at narrow submesoscales. On the other hand, for the frontolytic Leg D and E, the region from the north side to the center of the front is inferred to be dominated by upwelling, whereas downwelling is predicted on the south side of the front. The dominant upwelling in these transects may contribute to the formation of cold temperature mounds that convex upward on the north side of the front (Figures 16d and 16f). The submesoscale downwelling in the upper 100 m of the mixed layer front is seen in ω-equation solution on the south side of the front in Leg D and is consistent with the shallow low salinity tongue at the same location (Figure 6d).

5. Summary and Conclusion

[40] In this study, intensive surveys near the Kuroshio Front have been conducted using the microstructure profiler, LADCP, and CTD. Our observations suggest that the mixed layer south to the Kuroshio Front is in inertially and/or symmetrically unstable condition in fall 2009, because of the negative potential vorticity formed through the weak stratification and vertical and horizontal vorticity tilting on the anticyclonic side of the front. At these stations, because the cruise averaged wind is in the downfront direction, water can acquire negative PV value through frictional PV reduction driven by downfront wind stress at the surface of the front. Below the mixed layer, the PV is found to be near-zero in the tilted thermocline of the Kuroshio, which is formed by relatively weak stratification and large vertical shear at 220 m depth in 2008 data, suggesting that the Kuroshio Front thermocline is preconditioned for the symmetric instability. A similar tendency is found in the 2009 data.

[41] Direct observations of microscale turbulence show that turbulent dissipation rates are elevated in regions of the near-zero or negative PV in the mixed layer south of the front and in the thermocline under the mainstream of the Kuroshio. The scaling of the turbulent dissipation in the mixed layer shows that observed dissipation is an order of magnitude larger than the wind-scaling on the south side of the mixed layer front in Leg E, which can be scaled better using the empirical law considering wind and Ekman buoyancy flux. In contrast, the near-zero PV found in the thermocline (>150 m depth) of the Kuroshio Front is under the high PV layer (50–100 m depth), which may act as a barrier between the low PV water of the surface layers and that in the lower layers. At intermediate depths (>150 m) under the Kuroshio Front the low PV characteristics arise from weak stratification and vertical shear tilting term. The combination of the quasi-permanent shear, upstream intersection with topography, horizontal buoyancy gradient of the Kuroshio Front and the turbulent mixing, which we have repeatedly observed in the thermocline under the main stream of the Kuroshio Front,

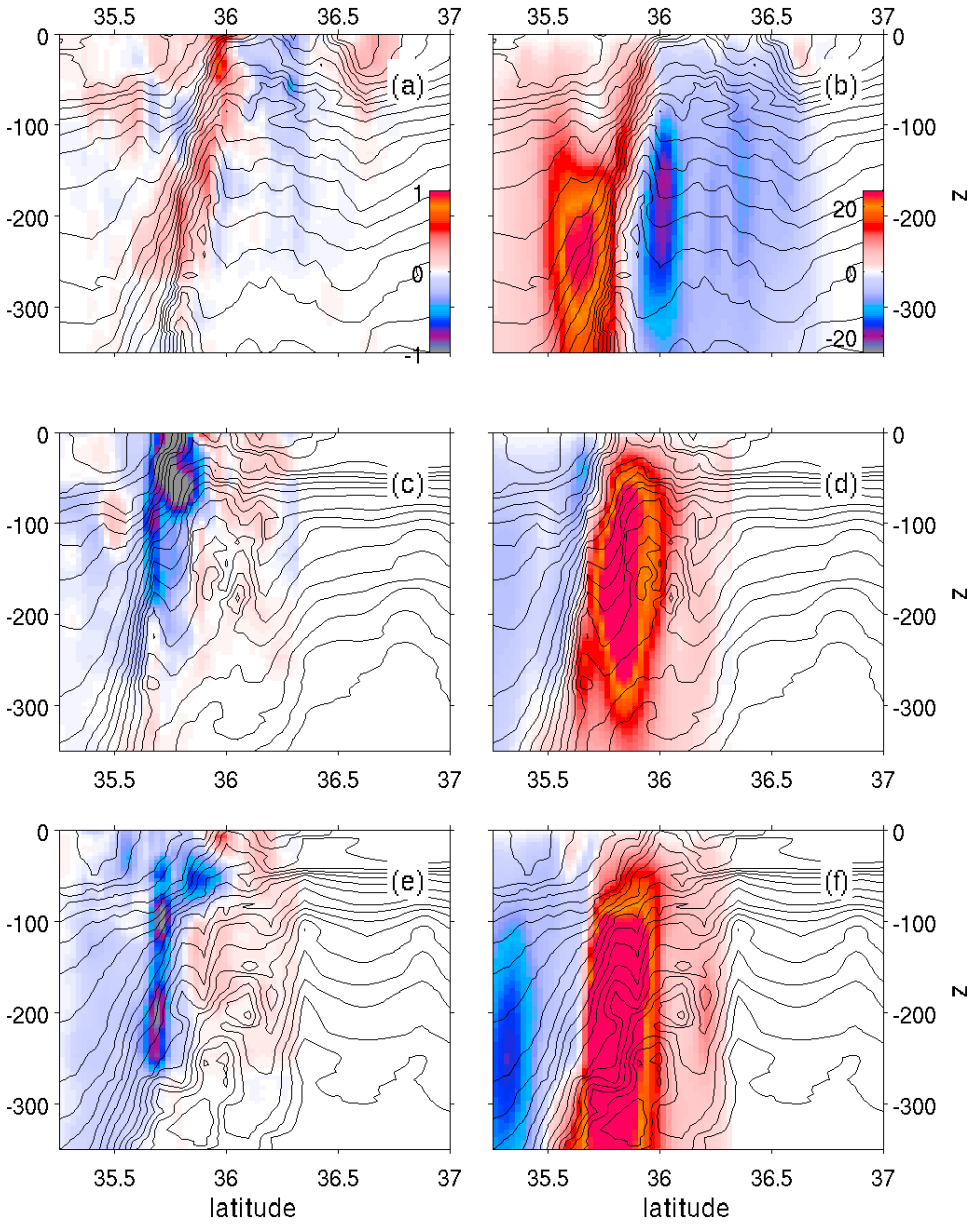

Figure 16. Vertical section of (left) frontogenesis function equation (7) $\times$ 10^{11} s^{-3} and (right) vertical velocity ($mday^{-1}$) inverted using (6) for (a, b) Leg A, (c, d) Leg D, and (e, f) Leg E. Black contours show temperature isotherms. The vertical sections of the frontogenesis function are smoothed using 12 m and 22 km running averages, in the vertical and horizontal direction.

could potentially lead to the patches of low PV arising near topography and advecting into the observed region where PV is being reset to zero by instabilities and subsequent mixing.

[42] Away from the Kuroshio mainstream, relatively strong coherent shear was observed both on the north side and south side of the Kuroshio Front, which cannot be seen in the corresponding geostrophic shear. Relatively strong turbulent dissipation observed in such regions were not associated with low background Ri_g (Figures 10 and 13). The rotary shear spectra show that these shear bands are attributed to downward propagations of near-inertial waves (Figure 12). Near-inertial waves are known to be trapped in anticyclonic regions with small effective Coriolis parameter, $\sqrt{f^2 - fu_y}$ [*Kunze*, 1985]. The non-geostrophic shear and relatively strong turbulence observed on the south side of the Kuroshio in Leg A, and E below the mixed layer (Figures 10, 11, and 12) support this scenario.

[43] Observed turbulent dissipation rates averaged in shear squared (S^2), and vertical buoyancy gradient (N^2) illustrate that the high turbulent dissipation could be categorized into two groups in terms of the two sources of the turbulent mixing mentioned above, namely, unbalanced ageostrophic flows near fronts, and the internal waves. Both of these groups are found near the front (Figure 13), suggesting that the frontal regions are sites of enhanced microscale turbulent dissipation. The combination of the diabatic turbulence and the adiabatic subduction near the Kuroshio Front is found to be important for diapycnal mixing of water masses, which could contribute

to the formation of the intermediate water masses (Figure 14). Although the frontal regions are very narrow, as the fronts are ubiquitous near the numerous eddies found in the Kuroshio-Oyashio confluent region, this combination provides a direct pathway to form subsurface salinity minima of North Pacific Intermediate Water in the entire North Pacific. Our microstructure data show intense turbulent mixing with an order of magnitude larger dissipation rate than that of the wind-scaling, which occurs in the inertially and/or symmetrically unstable mixed layer south of the Kuroshio Front, implying that these instabilities play a role in the formation of the STMW in winter.

[44] **Acknowledgments.** We acknowledge Captain Y. Kurita and crew on R.T.V. Umitaka, and Captain E. Ukekura and crew on R.V. Natsushima for ship operations; all the participants of two cruises for their contributions to the field surveys; and Amala Mahadevan and Gualtiero Badin for valuable discussions. The comments by John Taylor, Leif Thomas and an anonymous reviewer are greatly acknowledged. This study is supported by Sasagawa Scientific Research grant 20-701M (the Japan Science Society), Grant- in-Aid for Young Scientists (B) 20710002, and Excellent Young Researchers Overseas Visit Program 21-7283 awarded to T. Nagai. The latter grant and College of Engineering at UMass Dartmouth are acknowledged for T. Nagai's visit to UMass Dartmouth on sabbatical during the analysis phase of the Kuroshio observations. A. Tandon would like to acknowledge support from NSF-PO-0928138 and ONR N00014-09-1-0196.

References

Bluestein, H. B. (1993), *Synoptic-Dynamic Meteorology in Midlatitudes*, vol. II, *Observations and Theory of Weather Systems*, 594 pp., Oxford Univ. Press, Oxford, U. K.

Boccaletti, G., R. Ferrari, and B. Fox-Kemper (2007), Mixed layer instabilities and restratification, *J. Phys. Oceanogr.*, *37*, 2228–2250.

Bower, A. S. (1989), Potential vorticity balances and horizontal divergence along particle trajectories in Gulf Stream meanders east of Cape Hatteras, *J. Phys. Oceanogr.*, *19*, 1669–1681.

Brainerd, K. E., and M. C. Gregg (1993), Diurnal restratification and turbulence in the oceanic surface mixed layer: 1. Observations, *J. Geophys. Res.*, *98*, 22,645–22,656.

Capet, X., J. C. McWilliams, M. J. Molemaker, and A. F. Shchepetkin (2008a), Mesoscale to submesoscale transition in the California Current System. Part I: Flow structure, eddy flux, and observational tests, *J. Phys. Oceanogr.*, *38*, 29–43.

Capet, X., J. C. McWilliams, M. J. Molemaker, and A. F. Shchepetkin (2008b), Mesoscale to submesoscale transition in the California Current System. Part II: Frontal processes, *J. Phys. Oceanogr.*, *38*, 44–64.

Capet, X., J. C. McWilliams, M. J. Molemaker, and A. F. Shchepetkin (2008c), Mesoscale to submesoscale transition in the California Current System. Part III: Energy balance and flux, *J. Phys. Oceanogr.*, *38*, 2256–2269.

D'Asaro, E., C. Lee, L. Rainville, L. Harcourt, and L. Thomas (2011), Enhanced turbulence and energy dissipation at ocean fronts, *Science*, *332*, 318–322.

Dewey, R. K., and J. N. Moum (1990), Enhancement of fronts by vertical mixing, *J. Geophys. Res.*, *95*(C6), 9433–9445.

Doubell, M. J., H. Yamazaki, H. Li, and Y. Kokubu (2009), An advanced laser-based fluorescence microstructure profiler (TurboMAP-L) for measuring bio-physical coupling in aquatic systems, *J. Plankton Res.*, *31*, 441–452.

Fairall, C. W., E. F. Bradley, J. Godfrey, G. A. Wick, J. B. Edson, and G. Young (1996), Cool-skin and warm-layer effects on sea surface temperature, *J. Geophys. Res.*, *101*, 1295–1308.

Fischer, J., and M. Visbeck (1993), Deep velocity profiling with self-contained ADCPs, *J. Atmos. Oceanic Technol.*, *10*, 764–773.

Fox-Kemper, B., and R. Ferrari (2008), Parameterization of mixed layer eddies. Part II: Prognosis and impact, *J. Phys Oceanogr.*, *38*(6), 1166–1179, doi:10.1175/2007JPO3788.1.

Fox-Kemper, B., R. Ferrari, and R. W. Hallberg (2008), Parameterization of mixed layer eddies. Part I: Theory and diagnosis, *J. Phys Oceanogr.*, *38*(6), 1145–1165, doi:10.1175/2007JPO3792.1.

Franks, P. J. S., and L. J. Walstad (1997), Phytoplankton patches at fronts: A model of formation and response to wind events, *J. Mar. Res.*, *55*, 1–30.

Garrett, C. J. R., and J. W. Loder (1981), Dynamical aspects of shallow sea fronts, *Philos. Trans. R. Soc. London, Ser. A*, *1981*, 563–581.

Giordani, H., L. Prieur, and G. Caniaux (2006), Advanced insights into sources of vertical velocity in the ocean, *Ocean Dynamics*, *56*, 513–524.

Gregg, M. C. (1989), Scaling turbulent dissipation in the thermocline, *J. Geophys. Res.*, *94*, 9686–9698.

Gregg, M. C., and T. B. Sanford (1980), Signatures of mixing from Bermuda slope, the Sargasso Sea and the Gulf Stream, *J. Phys. Oceanogr.*, *10*, 105–127.

Hasegawa, D., H. Yamazaki, R. G. Lueck, and L. Seuront (2004), How islands stir and fertilize the upper ocean, *Geophys. Res. Lett.*, *31*, L16303, doi:10.1029/2004GL020143.

Haynes, P. H., and M. E. McIntyre (1987), On the evolution of vorticity and potential vorticity in the presence of diabatic heating and friction or other forces, *J. Atmos. Sci.*, *44*, 828–841.

Hoskins, B. J., and F. P. Bretherton (1972), Atmospheric frontogenesis models: Mathematical formulation and solution, *J. Atmos. Sci.*, *29*, 11–37.

Inoue, R., M. Gregg, and R. Harcourt (2010), Mixing rates across the Gulf Stream, part I: On the formation of Eighteen Degree Water, *J. Mar. Res.*, *68*, 643–671.

Iwamatsu, I., H. Yamazaki, T. Ishimaru, K. Kihara, Y. Koike, A. Kitazawa, and T. Hayashi (2003), An observation of low salinity water masses adjacent to the Kuroshio Front, *Uminokenkyu*, *12*, 477–486.

Johnston, J. M. S., D. L. Rudnick, and E. Pallás-Sanz (2011), Elevated mixing at a front, *J. Geophys. Res.*, *116*, C11033, doi:10.1029/2011JC007192.

Joyce, T. M., L. N. Thomas, and F. Bahr (2009), Wintertime observations of Subtropical Mode Water formation within the Gulf Stream, *Geophys. Res. Lett.*, *36*, L02607, doi:10.1029/2008GL035918.

Kouketsu, S., I. Yasuda, and Y. Hiroe (2005), Observation of frontal waves and associated salinity minimum formation along the Kuroshio Extension, *J. Geophys. Res.*, *110*, C08011, doi:10.1029/2004JC002862.

Kunze, E. (1985), Near-inertial wave propagation in geostrophic shear, *J. Phys. Oceanogr.*, *15*, 544–565.

Lévy, M., P. Klein, and G. Madec (2001), Impacts of sub-mesoscale physics on phytoplankton production and subduction, *J. Mar. Res.*, *59*, 535–565.

Lombardo, C. P., and M. C. Gregg (1989), Similarity scaling of viscous and thermal dissipation in a convecting surface boundary layer, *J. Geophys. Res.*, *94*, 6273–6284.

MacKinnon, J. A., and M. C. Gregg (2003), Mixing on the late-summer New England shelf-solibores, shear, and stratification, *J. Phys Oceanogr.*, *33*, 1476–1492.

Mahadevan, A., and D. Archer (2000), Modeling the impact of fronts and mesoscale circulation on the nutrient supply and biogeochemistry of the upper ocean, *J. Geophys. Res.*, *105*, 1209–1225.

Mahadevan, A., A. Tandon, and R. Ferrari (2010), Rapid changes in mixed layer stratification driven by submesoscale instabilities and winds, *J. Geophys. Res.*, *115*, C03017, doi:10.1029/2008JC005203.

Marshall, J. C., and A. J. G. Nurser (1992), Fluid dynamics of oceanic thermocline ventilation, *J. Phys. Oceanogr.*, *22*, 583–595.

McWilliams, J. C. (2008), Fluid dynamics at the margin of rotational control, *Environ. Fluid Mech.*, *8*, 441–449.

McWilliams, J. C., M. J. Molemaker, and E. I. Olafsdottir (2009), Linear fluctuation growth during frontogenesis, *J. Phys Oceanogr.*, *39*, 3111–3129.

Molemaker, M. J., J. C. McWilliams, and I. Yavneh (2005), Baroclinic instability and loss of balance, *J. Phys. Oceanogr.*, *35*, 1505–1517.

Molemaker, M. J., J. C. McWilliams, and X. Capet (2010), Balanced and unbalanced routes to dissipation in an equilibrated eady flow, *J. Fluid Mech*, *654*, 35–63.

Nagai, T., A. Tandon, and D. L. Rudnick (2006), Two-dimensional ageostrophic secondary circulation at ocean fronts due to vertical mixing and large-scale deformation, *J. Geophys. Res.*, *111*, C09038, doi:10.1029/2005JC002964.

Nagai, T., A. Tandon, N. Gruber, and J. C. McWilliams (2008), Biological and physical impacts of ageostrophic frontal circulations driven by confluent flow and vertical mixing, *Dyn. Atmos. Ocean*, *45*, 229–251.

Nagai, T., A. Tandon, H. Yamazaki, and M. J. Doubell (2009), Evidence of enhanced turbulent dissipation in the frontogenetic Kuroshio Front thermocline, *Geophys. Res. Lett.*, *36*, L12609, doi:10.1029/2009GL038832.

Nasmyth, P. W. (1970), Oceanic turbulence, Ph.D. thesis, Univ. of B. C., Vancouver, B. C., Canada.

Oakey, N. S. (1982), Determination of the rate of dissipation of turbulent energy from simultaneous temperature and velocity shear microstructure measurements, *J. Phys. Oceanogr.*, *12*, 256–271.

Oakey, N. S., and J. A. Elliot (1977), Vertical temperature gradient structure across the Gulf Stream, *J. Geophys. Res.*, *82*, 1369–1380.

Osborn, T. (1980), Estimates of the local rate of vertical diffusion from dissipation measurements, *J. Phys. Oceanogr.*, *10*, 83–89.

Pallás-Sanz, E., T. M. S. Johnston, and D. L. Rudnick (2010a), Frontal dynamics in a California Current System shallow front: 1. Frontal processes and tracer structure, *J. Geophys. Res.*, *115*, C12067, doi:10.1029/2009JC006032.

Pallás-Sanz, E., T. M. S. Johnston, and D. L. Rudnick (2010b), Frontal dynamics in a California Current System shallow front: 2. Mesoscale vertical velocity, *J. Geophys. Res.*, *115*, C12068, doi:10.1029/2010JC006474.

Plougonven, R., and C. Snyder (2007), Inertia-gravity waves spontaneously generated by jets and fronts. Part I: Different baroclinic life cycles, *J. Atmos. Sci.*, *64*, 2502–2520.

Pollard, R. T., and L. A. Regier (1992), Vorticity and vertical circulation at an ocean front, *J. Phys. Oceanogr.*, *22*, 609–625.

Qiu, B., and S. Chen (2006), Decadal variability in the formation of the North Pacific Subtropical Mode Water: Oceanic versus atmospheric control, *J. Phys. Oceanogr.*, *36*, 1365–1380.

Rainville, L., and R. Pinkel (2004), Observations of energetic high-wavenumber internal waves in the Kuroshio, *J. Phys. Oceanogr.*, *34*, 1495–1505.

Rudnick, D. L. (1996), Intensive surveys of the Azores front. Part II: Inferring the geostrophic and vertical velocity fields, *J. Geophys. Res.*, *101*, 16,291–16,303.

Shcherbina, A., Y. Lynne, D. Talley, E. Firing, and P. Hacker (2003), Near-surface frontal zone trapping and deep upward propagation of internal wave energy in the Japan/East Sea, *J. Phys. Oceanogr.*, *33*, 900–912.

Taylor, J. R., and R. Ferrari (2009), On the equilibration of a symmetrically unstable front via a secondary shear instability, *J. Fluid Mech.*, *622*, 103–113.

Taylor, J. R., and R. Ferrari (2010), Buoyancy and wind-driven convection at mixed layer density fronts, *J. Phys. Oceanogr.*, *40*, 1222–1242.

Terray, E. A., M. A. Donelan, Y. C. Agrawal, W. M. Drennan, K. K. Kahma, A. J. Williams, P. A. Hwang, and S. A. Kitaigorodskii (1996), Estimates of kinetic energy dissipation under breaking waves, *J. Phys. Oceanogr.*, *26*, 792–807.

Thomas, L., and J. R. Taylor (2010), Reduction of the usable wind-work on the general circulation by forced symmetric instability, *Geophys. Res. Lett.*, *37*, L18606, doi:10.1029/2010GL044680.

Thomas, L. N. (2005), Destruction of potential vorticity by winds, *J. Phys. Oceanogr.*, *35*, 2457–2466.

Thomas, L. N. (2008), Formation of intrathermocline eddies at ocean fronts by wind-driven destruction of potential vorticity, *Dyn. Atmos. Oceans*, *45*, 252–273.

Thomas, L. N., and R. Ferrari (2008), Friction, frontogenesis, and the stratification of the surface mixed layer, *J. Phys. Oceanogr.*, *38*, 2501–2518.

Thomas, L. N., and C. M. Lee (2005), Intensification of ocean fronts by down-front winds, *J. Phys. Oceanogr.*, *35*, 1086–1102.

Thomas, L. N., A. Tandon, and A. Mahadevan (2008), Submesoscale processes and dynamics, in *Ocean Modeling in an Eddying Regime*, *Geophys. Monogr. Ser.*, vol. 177, edited by M. Hecht and H. Hasumi, pp. 17–38, AGU, Washington, D. C.

Thompson, L. (2000), Ekman layers and two-dimensional frontogenesis in the upper ocean, *J. Geophys. Res.*, *105*, 6437–6451.

Uda, M. (1936), Locality of fishing centre and shoals of "Katsuwo", Euthynnus Vagans (Lesson), correlated with the contact zone of cold and warm currents, *Bull. Jpn. Soc. Sci. Fish.*, *4*, 385–390.

Winkel, D. P., M. C. Gregg, and T. B. Sanford (2002), Patterns of shear and turbulence across the Florida Current, *J. Phys Oceanogr.*, *32*, 3269–3285.

Yasuda, I. (2004), North Pacific Intermediate Water: Progress in SAGE (SubArctic Gyre Experiment) and related projects, *J. Oceanogr.*, *60*, 385–395.